



# Paleoceanography and Paleoclimatology

## RESEARCH ARTICLE

10.1029/2020PA003957

### Special Section:

Community Earth System Model Version 2 (CESM2) Special Collection

### Key Points:

- Orbital configurations for 6 ka and 127 ka force enhanced Northern Hemisphere summer insolation versus the preindustrial, with greater anomalies at 127 ka
- This forcing in CESM2 yields summer warming over Northern Hemisphere continents, reduced Arctic minimum sea ice, and increased extent of the North African monsoon
- The middle Holocene and Last Interglacial simulations provide out-of-sample tests of CESM2

### Supporting Information:

- Supporting Information S1

### Correspondence to:

B. L. Otto-Bliesner, [ottobli@ucar.edu](mailto:ottobli@ucar.edu)

### Citation:

Otto-Bliesner, B. L., Brady, E. C., Tomas, R. A., Albani, S., Bartlein, P. J., Mahowald, N. M., et al. (2020). A comparison of the CMIP6 *midHolocene* and *lig127k* simulations in CESM2. *Paleoceanography and Paleoclimatology*, 35, e2020PA003957. <https://doi.org/10.1029/2020PA003957>

Received 12 MAY 2020

Accepted 6 OCT 2020

Accepted article online 16 OCT 2020

## A Comparison of the CMIP6 *midHolocene* and *lig127k* Simulations in CESM2

Bette L. Otto-Bliesner<sup>1</sup> , Esther C. Brady<sup>1</sup> , Robert A. Tomas<sup>1</sup>, Samuel Albani<sup>2</sup> , Patrick J. Bartlein<sup>3</sup> , Natalie M. Mahowald<sup>4</sup> , Sarah L. Shafer<sup>5</sup> , Erik Kluzek<sup>1</sup> , Peter J. Lawrence<sup>1</sup> , Gunter Leguy<sup>1</sup> , Mathew Rothstein<sup>1</sup>, and Aleah N. Sommers<sup>1</sup>

<sup>1</sup>Climate and Global Dynamics Laboratory, National Center for Atmospheric Research, Boulder, CO, USA, <sup>2</sup>Department of Environmental and Earth Sciences, University of Milano-Bicocca, Milan, Italy, <sup>3</sup>Department of Geography, University of Oregon, Eugene, OR, USA, <sup>4</sup>Department of Earth and Atmosphere Sciences, Cornell University, Ithaca, NY, USA, <sup>5</sup>U.S. Geological Survey, Corvallis, OR, USA

**Abstract** Results are presented and compared for the Community Earth System Model version 2 (CESM2) simulations of the middle Holocene (MH, 6 ka) and Last Interglacial (LIG, 127 ka). These simulations are designated as Tier 1 experiments (*midHolocene* and *lig127k*) for the Coupled Model Intercomparison Project phase 6 (CMIP6) and the Paleoclimate Modeling Intercomparison Project phase 4 (PMIP4). They use the low-top, standard 1° version of CESM2 contributing to CMIP6 DECK, historical, and future projection simulations, and to other modeling intercomparison projects. The *midHolocene* and *lig127k* provide the opportunity to examine the responses in CESM2 to the orbitally induced changes in the seasonal and latitudinal distribution of insolation. The insolation anomalies result in summer warming over the Northern Hemisphere continents, reduced Arctic summer minimum sea ice, and increased areal extent of the North African monsoon. The Arctic remains warm throughout the year. These changes are greater in the *lig127k* than *midHolocene* simulation. Other notable changes are reduction of the Niño3.4 variability and Drake Passage transport and a small increase in the Atlantic Meridional Overturning Circulation from the *piControl* to *midHolocene* to *lig127k* simulation. Comparisons to paleo-data and to simulations from previous model versions are discussed. Possible reasons for mismatches with the paleo-observations are proposed, including missing processes in CESM2, simplifications in the CMIP6 protocols for these experiments, and dating and calibration uncertainties in the data reconstructions.

**Plain Language Summary** The modeling of past climates, using physically based tools and comparing to paleo-observations, is increasingly seen as a strong test of the models that are used for the projection of future climate changes. We report on simulations by one of the latest large-scale climate models, the Community Earth System Model version 2 (CESM2), for the two most recent warm epochs: the current interglacial—the Holocene, which began 11,650 years ago - and the previous interglacial—the Last Interglacial, which extended from 129,000 to 116,000 years ago. The simulations find summer warming over the Northern Hemisphere continents, reduced Arctic summer sea ice, and increased areal extent of the North African monsoon. Cryospheric and oceanic feedbacks drive year-round Arctic warmth. The CESM2 middle Holocene and Last Interglacial simulations are an important resource for the community participating in the Coupled Model Intercomparison Project phase 6 (CMIP6).

## 1. Introduction

The modeling of paleoclimate in the Coupled Model Intercomparison Project (CMIP) and the Paleoclimate Modeling Intercomparison Project (PMIP) has long been used to understand and explain past environmental change (Braconnot et al., 2007, 2012; Joussaume et al., 1999) and as out-of-sample tests of models being used for projections of future climate (Folland et al., 1990; Jansen et al., 2007; Masson-Delmotte et al., 2013; McAvaney et al., 2001).

The middle Holocene (MH, 6 ka) has been a target of PMIP since its first phase using atmosphere only models because of evidence from data of warmer Northern Hemisphere (NH) summers and enhanced NH monsoons (COHMAP Members, 1988; Harrison et al., 1998) in response to enhanced summer insolation associated with the shift of perihelion to near the boreal autumn equinox as compared to near the boreal

©2020. The Authors.

This is an open access article under the terms of the Creative Commons Attribution License, which permits use, distribution and reproduction in any medium, provided the original work is properly cited.

winter solstice at present (Berger & Loutre, 1991; Otto-Bliesner et al., 2017). A wide variety of archives have been analyzed since then to reconstruct additional climate variables, including lake levels (Coe & Harrison, 2002), growing degree days (Bartlein et al., 2011), biomass burning (Power et al., 2008), ENSO variability (Emile-Geay et al., 2016) and sea ice (Stein, Fahl, Schade, et al., 2017). The *midHolocene* is considered Tier 1 within CMIP6 and one of two paleoclimate experiments, with the Last Glacial Maximum (LGM), that serves as an entry card to PMIP4 along with a CMIP6 DECK preindustrial (PI) experiment as a paired control (Eyring et al., 2016; Kageyama et al., 2018).

For the first time, the Last Interglacial (LIG, 127 ka) has been included as a Tier 1 CMIP6-PMIP4 experiment to allow the assessment of model simulations for that warm period in the IPCC AR6 (Intergovernmental Panel on Climate Change Sixth Assessment Report; Otto-Bliesner et al., 2017). Previously, LIG simulations were made with older and/or lower-resolution versions of the models than were used for future projections (Lunt et al., 2013). Differences in these LIG simulations could also have arisen because of differences in the experimental designs: the orbital forcing and GHG concentrations varied among the simulations. Several reasons were given at the 2015 Cambridge PAGES QUIGS workshop for identifying a 127 ka time slice for the CMIP6-PMIP4 LIG experiment: Northern Hemisphere seasonal insolation anomalies are large with perihelion near boreal summer solstice, little or no remnants of the North American and Eurasian ice sheets, and sufficient time elapsed to minimize the imprint of the earlier deglaciation and Heinrich 11 (H11) melt-water event given dating uncertainties (Marino et al., 2015; Otto-Bliesner et al., 2017). For CMIP6-PMIP4, a common protocol was established for participating modeling groups to run with the same model and at the same resolution as their DECK simulations if participating in CMIP6 or their preindustrial control simulations if only participating in PMIP4 (Otto-Bliesner et al., 2017).

The family of CESM models (CSM1, CCSM3, CCSM4) have simulated the MH, starting with atmosphere-only simulations with fixed present-day sea surface temperatures (CSM1, Otto-Bliesner, 1999), low-resolution coupled atmosphere–ocean simulations (CCSM3, Otto-Bliesner et al., 2006), and coupled atmosphere–ocean simulations in CMIP5 with CCSM4 run at the same resolution (FV1x1) as the preindustrial, historical and future projections. CCSM4 experiments were also completed for the Last Glacial Maximum (LGM, Brady et al., 2013), Last Millennium (LM, Landrum et al., 2013), Last Interglacial, and mid-Pliocene Warm Period (mPWP, Rosenbloom et al., 2013) to understand the model response of the climate system to different climate forcings for documented states very different from the present and historical.

In this paper, we provide a short summary of the model components in Section 2 (for more details see Danabasoglu et al., 2020) and the experimental design in Section 3. In Section 4 we provide an analysis of the responses of CESM2 to the orbitally induced changes in insolation on the atmosphere, ocean, sea ice, and land. We compare and contrast the responses between the *midHolocene* and *lig127k* with their differences in the phasing and magnitudes of the seasonal and latitudinal distribution of insolation anomalies in terms of mean climate and climate variability. Comparison to previous modeling results from the family of CESM models and proxy reconstructions is included in Section 5.

## 2. Model Description

The CESM2 is a coupled model consisting of components for the atmosphere (CAM6, WACCM6), ocean (POP2), sea ice (CICE5), land (CLM5), and land ice (CISM2). We briefly summarize the component models relevant to our *midHolocene* and *lig127k* simulations. More details on each of these components, their coupling, and the science improvements can be found in Danabasoglu et al. (2020).

The low-top atmosphere model, the Community Atmosphere Model version 6 (CAM6) is used for the CESM2 *midHolocene* and *lig127k* simulations. CAM6 has a nominal  $1^\circ$  ( $1.25^\circ$  in longitude and  $0.9^\circ$  in latitude) horizontal resolution. There are 32 vertical levels with the top at 2.26 hPa (about 40 km): 7 levels below 850 hPa, 10 levels between 850 and 200 hPa, and 15 levels above 200 hPa. It includes the four-mode Modal Aerosol Model (MAM4; Liu et al., 2016). A two-moment cloud microphysics scheme (MG2, Gettelman & Morrison, 2015) explicitly models the cloud-aerosols interactions, allowing for the inclusion of the indirect effects of aerosols. The Cloud Layers Unified by Binormals (CLUBB) is now used for representation of shallow convection, boundary layer, and grid-scale condensation (Bogenschutz et al., 2013). The orographic drag parameterizations have also been updated.

The ocean model is the Parallel Ocean Program version 2 (POP2), the same as in CCSM4 but with improvements in some physical parameterizations, including an estuary balance model for better handling of runoff from the land model and increased mesoscale diffusivities at depth to improve the representation of passive tracers. The ocean model also simulates ocean biogeochemistry (MARBL), including multiple nutrient co-limitation (N, P, Si, Fe) and three explicit phytoplankton (diatoms, diazotrophs, pico/nano phytoplankton), one implicit group (calcifiers), and one zooplankton group. The horizontal resolution is a nominal  $1^\circ$  with a uniform resolution of  $1.125^\circ$  in the zonal direction. The North Pole is displaced into Greenland. The meridional resolution is variable:  $0.27^\circ$  at the equator; increasing monotonically to  $0.53^\circ$  at  $32^\circ\text{S}$ , then constant farther south;  $0.38^\circ$  in the northwestern Atlantic Ocean and  $\sim 0.64^\circ$  in the northwestern Pacific Ocean. There are 60 vertical levels with a maximum depth of 5,500 m. The upper 16 vertical levels have a uniform thickness of 10 m. Below  $\sim 160$  m depth, the level thicknesses increase monotonically to  $\sim 3,500$  m depth. The deepest 2000 m have a nearly uniform thickness of  $\sim 250$  m extending to the bottom at  $\sim 5,500$  m.

The sea ice model is CICE version 5 (Hunke et al., 2015), now incorporating mushy-layer thermodynamics and an updated melt pond scheme. It uses the same horizontal grid as the ocean model.

The land model is the Community Land Model version 5 (CLM5), with extensive improvements to the model's hydrological and ecological parameterizations. Its horizontal grid is the same as the atmospheric model. Atmospheric dust is mobilized from the land. Factors for determining soil erodibility and dust emission include the wind friction speed, vegetation cover, and soil moisture (Mahowald et al., 2006; Zender et al., 2003). All other aerosol emissions in our *lig127k* and *midHolocene* simulations are prescribed as in the *piControl* simulation as given by the CMIP6 datasets. A new river model (Model for Scale Adaptive River Transport, MOSART) is included, which simulates streamflow, time-varying channel velocities, channel water depth, and channel surface water variations.

The land-ice model is the Community Ice Sheet Model version 2.1 (CISM2.1), based on the Glimmer-CISM model, and includes a three-dimensional thermodynamical model and high-order velocity solver. It currently runs for Greenland on a 4-km grid. For the *midHolocene* and *lig127k* simulations, CISM2.1 is set to NO-EVOLVE, i.e. a fixed Greenland ice sheet. The Greenland ice sheet Surface Mass Balance (SMB) and surface temperature are downscaled from the 10-virtual elevation classes calculated in the land model to the 4-km CISM grid, allowing for future use in ice sheet-only simulations (Lipscomb et al., 2013).

### 3. Experimental Design and Methods

The CESM2 (CAM6) *midHolocene* and *lig127k* simulations use the CESM2.1.0 released version. We adopt the forcings and boundary conditions (Table 1) following the protocols of the Tier 1 experiments (*midHolocene* and *lig127k*) for CMIP6 and PMIP4, as defined in Otto-Bliesner et al. (2017), with two exceptions: vegetation and dust. Vegetation is prescribed as potential vegetation rather than preindustrial vegetation. The CESM2 interactive dust parameterization is modified to account for the influence on dust emissions exerted by the climate-induced changes in vegetation during the middle Holocene and Last Interglacial not included in our simulations with prescribed vegetation. These simulations are compared to the CESM2 CMIP6 *piControl* (see Eyring et al., 2016, and Danabasoglu et al., 2020, for details on the forcings, boundary conditions, and *piControl* simulation).

The Earth's orbital parameters (eccentricity, longitude of perihelion, and obliquity) are prescribed following Berger and Loutre (1991). These parameters affect the seasonal and latitudinal distribution and magnitude of solar energy received at the top of the atmosphere and, in the case of obliquity, the annual mean insolation at any given latitude. At 6 ka, the eccentricity is similar to PI but perihelion occurs near the boreal autumn equinox as compared to near the boreal winter solstice at PI. The orbit at 127 ka is characterized by larger eccentricity than at PI, and in addition perihelion occurs close to the boreal summer solstice. These orbital configurations result in large positive NH summer insolation anomalies at 6 ka and 127 ka as compared to PI (Figure 1). The anomalies are considerably greater at 127 ka than at 6 ka, associated with greater eccentricity and boreal summer solstice at perihelion at 127 ka.

Climate models generally adopt the modern calendar when outputting monthly averages. That is, the month lengths are fixed at their modern definitions. The altered orbit at 6 ka and 127 ka, as compared to PI, affects the Earth's transit speed along different parts of its orbit. So, for example, the number of days between the

**Table 1**  
Summary of Forcings and Boundary Conditions Used in the MidHolocene, lig127k, and piControl Simulations

Parameter setting	midHolocene	lig127k	piControl
<b>Orbit</b>	6 ka	127 ka	1850
<b>Solar</b>	Same as <i>piControl</i>	Same as <i>piControl</i>	Fixed SSI, 1850–1873 mean
<b>CO<sub>2</sub>(ppm)</b>	264.4	275.0	284.7 <sup>a</sup>
<b>CH<sub>4</sub>(ppb)</b>	597.0	685.0	791.6 <sup>a</sup>
<b>N<sub>2</sub>O(ppb)</b>	262.0	255.0	275.68 <sup>a</sup>
<b>Other GHG (CFCs)</b>	0.	0.	DECK <i>piControl</i>
<b>Ozone</b>	Same as <i>piControl</i>	Same as <i>piControl</i>	DECK <i>piControl</i>
<b>Volcanic aerosols</b>	Same as <i>piControl</i>	Same as <i>piControl</i>	Background 1850–2014 mean from WACCM ensemble
<b>Aerosols (excluding dust)</b>	DECK <i>piControl</i>	DECK <i>piControl</i>	DECK <i>piControl</i>
<b>Vegetation</b>	Potential Vegetation <sup>b</sup> , No urban, no crops	Potential Vegetation <sup>b</sup> , No urban, no crops	1850 CE Preindustrial Vegetation and crops
<b>Land Surface Topography</b>	Modern	Modern	Modern
<b>Soil Erodibility/Dust</b>	Modified <sup>c</sup>	Modified <sup>c</sup>	Modern
<b>Ice Sheets</b>	Modern	Modern	Modern
<b>#production years</b>	1–700	1–700	1,200
<b>#spin up years</b>	323	325	1,070

<sup>a</sup>Note that these GHG concentrations were set as in CMIP5 protocols and not as in the piControl CMIP6 DECK protocols which have CO<sub>2</sub> = 284.317 ppm, CH<sub>4</sub> = 808.25 ppb, N<sub>2</sub>O = 273.02 ppb. <sup>b</sup>Potential vegetation rather than the 1850 CE preindustrial vegetation used. The potential vegetation removes crops and urban areas (see Section 3 for more details). <sup>c</sup>Inputs to dust parameterization modified to account for the influence on dust emissions exerted by climate-induced changes in vegetation at 6 ka and 127 ka that are not included as boundary conditions in the CESM2 *midHolocene* and *lig127k* simulations (see Section 3 for more details)

NH summer solstice and the NH fall equinox is about 4 days and 7 days shorter than at PI for 6 ka and 127 ka, respectively (see Figure 2 in Otto-Bliesner et al., 2017). Conversely, the number of days between the NH winter solstice and the NH spring equinox get progressively longer from PI to 6 ka to 127 ka. The net effect is that NH winters (December, January, February, DJF) were longer and summers (June, July, August, JJA) shorter from an insolation perspective at 127 ka and 6 ka than at PI. Bartlein and Shafer (2019) illustrate that the impacts on temperature and precipitation anomaly patterns related to changes in the length of months is greatest from September to December for 6 ka, and all but January to May for 127 ka. The PaleoCalAdjust v1.0 of Bartlein and Shafer (2019) accounts for the impact of these changes in the length of months at 6 ka and 127 ka. In the analyses of CESM2 results, we use PaleoCalAdjust v1.0 to convert the outputted monthly averages to ‘celestial’ calendar months.

Vegetation cover is prescribed in the *midHolocene*, *lig127k*, and *piControl* simulations, though the leaf area index and vegetation height are prognostic and can be affected by the changed climate. The land cover in the *piControl* simulation merges present-day satellite land cover with the LUH2 data for primary and secondary forest and nonforest land units, five crop groups, managed pasture, rangeland, and urban areas at 1850 CE (Lawrence et al., 2019). To remove anthropogenic influences on the land surface for the *midHolocene* and *lig127k* simulations, a new “potential vegetation” distribution was derived from natural vegetation land units, such that historical crop and urban areas of CESM2 are replaced with suitable natural vegetation types reflecting the distribution of vegetation in the absence of human activity under preindustrial environmental conditions. Potential vegetation distributions were generated using the LUMIP Land Use Harmonization version 2 (LUH2) data (Lawrence et al., 2016) starting with the land use distribution for the year of 850 CE. Any agriculture present in that year was replaced by the nearest neighboring natural land unit, producing the potential vegetation LUH2 land unit distribution. The largest changes in agricultural land use compared to PI are in India, Europe and China (Figure 2 and Figure S1). The urban land cover was set to zero for all land points in keeping with the lack of significant built infrastructure at 6 ka and 127 ka.

In CESM2, soil erodibility maps provide a scaling factor on dust emission fluxes. It is a spatially varying parameter summarizing the differences in susceptibility to erosion related to, e.g. soil textures and geomorphology (Mahowald et al., 2006; Zender et al., 2003). The CESM2 *midHolocene* and *lig127k* simulations do not include changes in vegetation associated with the simulated changes in precipitation and temperature during these time intervals (i.e., we use prescribed near-modern, pre-anthropogenic vegetation). To account for

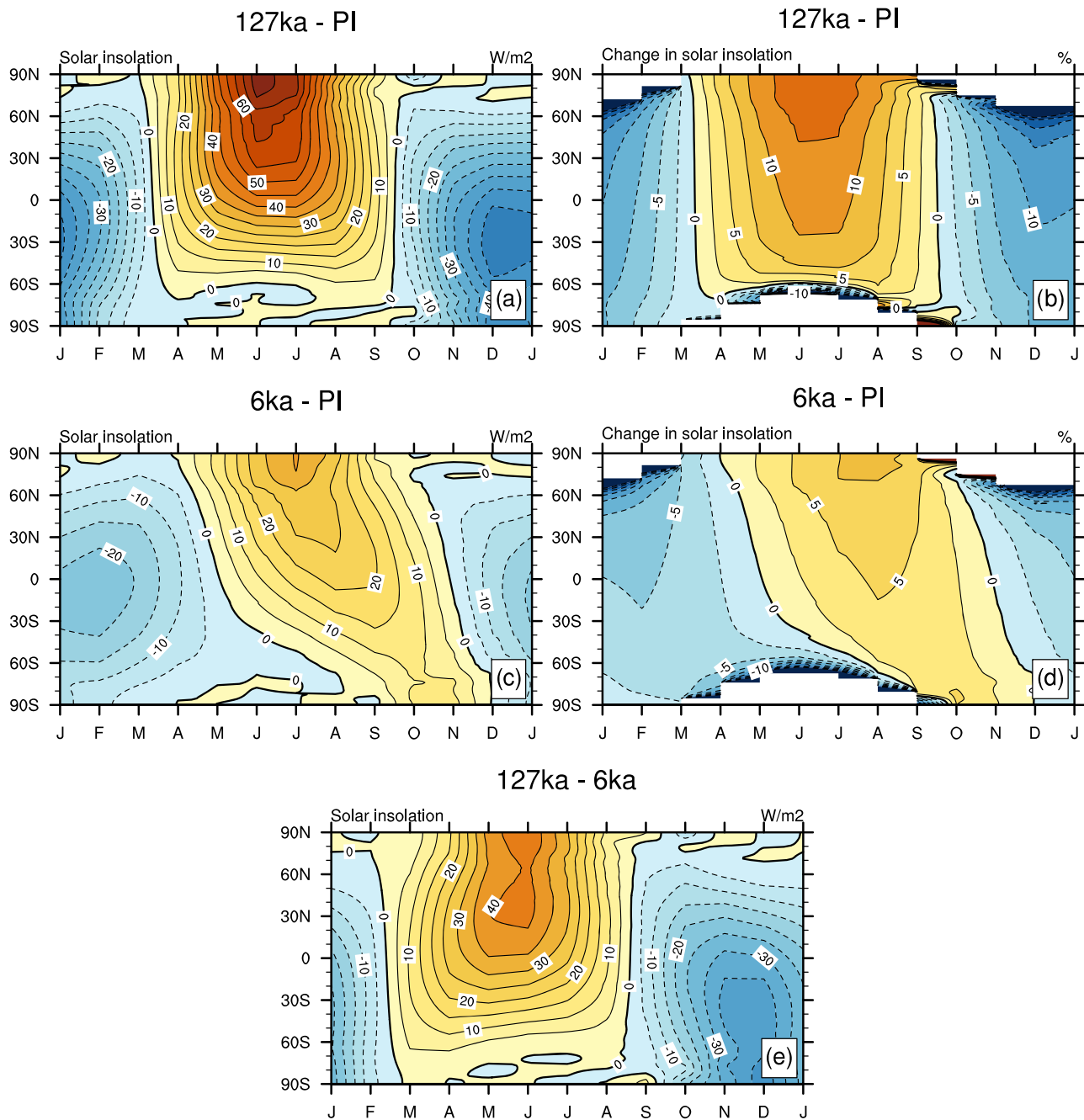


**Figure 1.** Seasonal cycle of insolation anomalies for the *midHolocene* and *lig127k* simulations. a), c), e)  $W m^{-2}$ ; b), d) percentage change from the *piControl*.

the influence on dust emissions exerted by changes in vegetation (Jolly et al., 1998), we performed offline simulations with the coupled biogeography and biogeochemistry equilibrium model (BIOME4) (Kaplan et al., 2003) to determine *midHolocene* vegetation, and use these results to determine the location of potential dust source areas, as well as the area of a grid box available for dust generation, assuming that the nonvegetated fractions of arid areas can lead to dust emissions (Mahowald et al., 2006). We then incorporated this as an additional information layer of the soil erodibility map, at the same time removing the dependence of dust mobilization on TLAI (Total Leaf Area Index) from the main code, which would use the preindustrial vegetation instead, as described in Albani et al. (2015). A second step involves

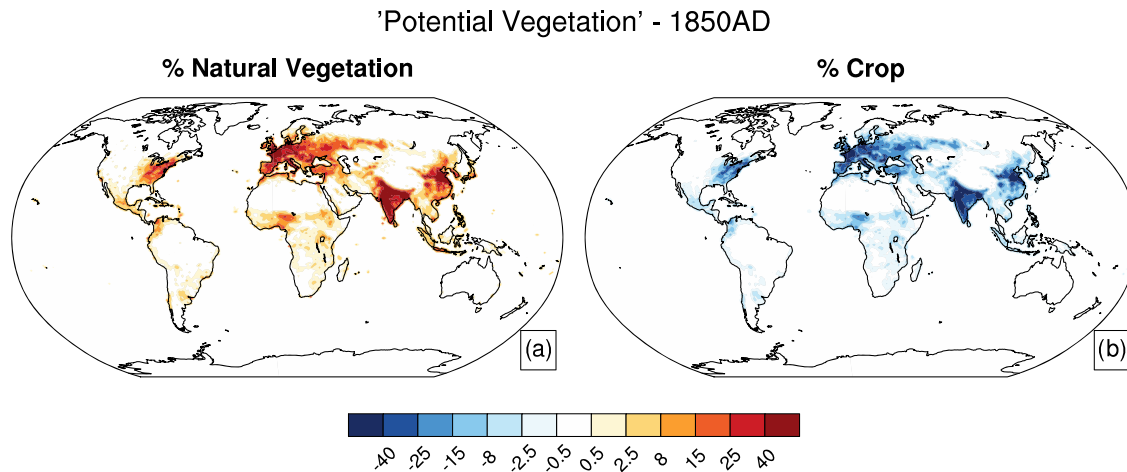


**Figure 2.** Potential vegetation in simulations. Percentages differences in a) natural vegetation and b) cropland landunits between the CESM2.1 PMIP4 “no-Anthro” potential vegetation and the *piControl* surface boundary conditions.

further refining, at the continental level, the soil erodibility map. A set of scale factors for the soil erodibility map is defined for different macro areas (i.e., continents), based on achieving the best fit of dust deposition from preliminary *midHolocene* simulations with CESM2 to an observational benchmark, i.e., dust mass accumulation rates from paleodust archives (Albani et al., 2015). The *midHolocene* soil erodibility map was also used in the *lig127k* simulation. Note that a change in the coarse mode aerosol definition (from a geometric sigma of 1.6 to 1.2) between CAM5 (Albani et al., 2014) and the CAM6 used here, results in a more negative dust direct radiative effect, no longer matching available observations. Further analyses investigating this aspect in more detail would be useful.

Records from Antarctica and Greenland ice cores indicate 6 ka and 127 ka concentrations of the well-mixed GHGs: CO<sub>2</sub>, CH<sub>4</sub>, and N<sub>2</sub>O comparable to, albeit somewhat lower than PI (Table 1). All other forcings and boundary conditions—solar constant, ozone, volcanic aerosols, topography and bathymetry, and ice sheets—in the *midHolocene* and *lig127k* simulations remain the same as in the *piControl* simulation.

## 4. Results

### 4.1. Atmosphere

#### 4.1.1. Surface Air Temperature

Both 6 ka and 127 ka show large NH positive insolation anomalies during boreal summer as compared to PI (Figure 1). The positive NH summer insolation anomalies at 6 ka force warming greater than 2 °C over the NH continents in June–July–August (JJA) in the *midHolocene* simulation, with some regions at mid-latitudes over Eurasia experiencing surface air temperature increases of more than 4 °C (Figure 3(f)). JJA warming over the NH continents in the *lig127k* simulation, associated with the much larger positive NH summer insolation anomalies, exhibit surface temperature increases approximately doubled as compared to 6 ka, to more than 4 °C to over 8 °C (Figure 3(e)). In the *lig127k* simulation, the response of surface air temperatures is more than just a NH response. The nature of the orbital parameters, with the positive insolation anomalies from April to September extending into the Southern Hemisphere (SH), results in considerable warming over South America, Australia, and southern Africa as well as in the Atlantic and Indian Ocean sectors of the Southern Ocean in the *lig127k* simulation. These responses are also reflected in JJA global and NH extratropical land averages (Table 2).

At 6 ka and 127 ka, negative insolation anomalies occur during December–January–February (DJF) as compared to PI (Figure 1). The continental and much of the oceanic regions in both hemispheres cool in response to the insolation forcing, with greater cooling in the *lig127k* simulation than the *midHolocene* simulation (Figure 3(c), 3(d)). The exceptions are the Arctic, high-latitude North Atlantic, and Atlantic and

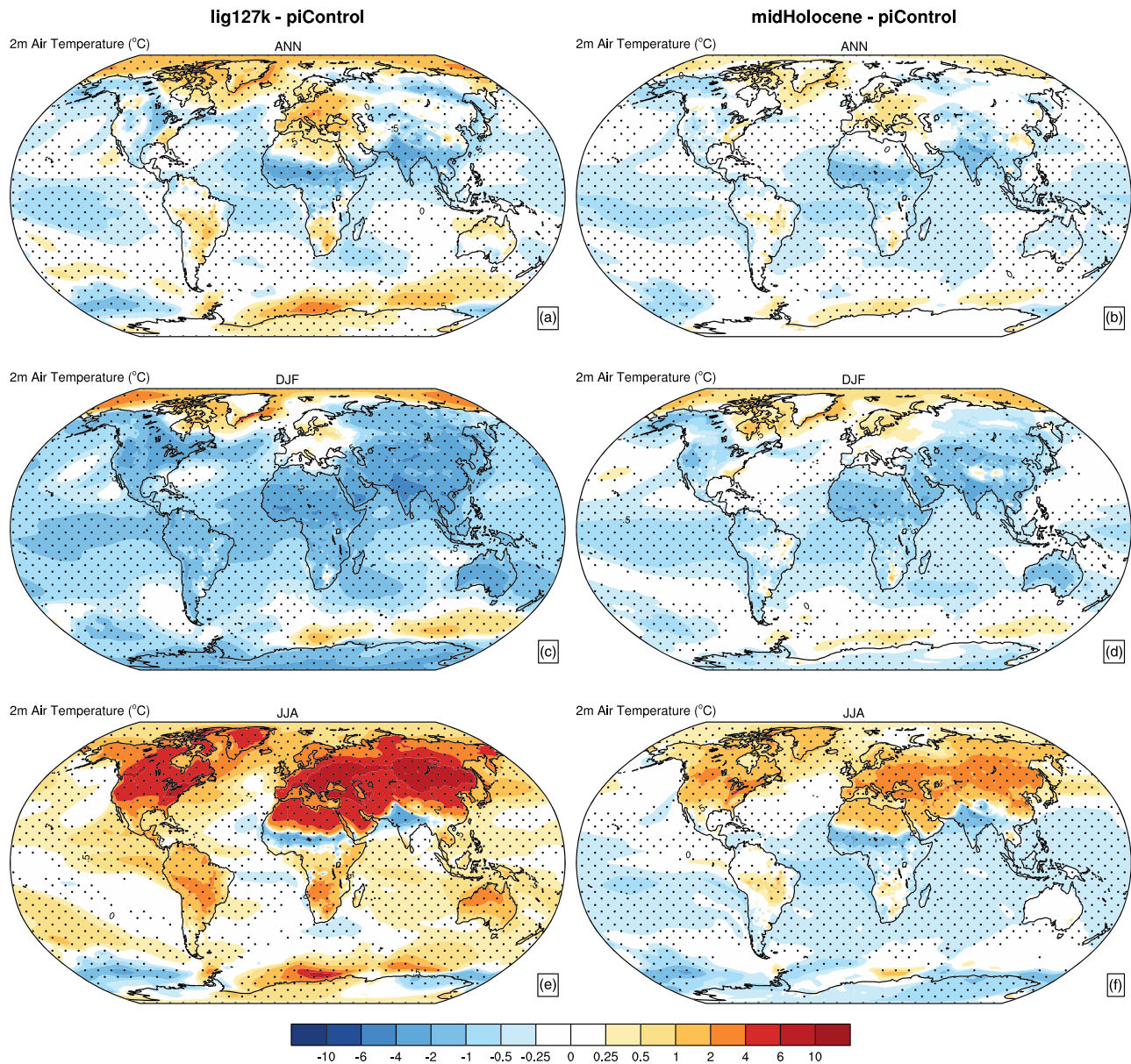


**Figure 3.** Annual and seasonal surface air temperature anomalies (°C) in the *lig127k* and *midHolocene* simulations as compared to the *piControl* simulation. Stippling indicates anomalies statistically significant at 95% level.

Indian Ocean sectors of the Southern Ocean, which remain warmer than PI. Positive feedbacks with the cryosphere (sea ice and snow cover) and ocean provide the memory that allows simulated high-latitude warming, in DJF as well as annually (Figure 3(a), 3(b)).

While the largest anomalies in surface air temperature appear seasonally, there is a consistent pattern of weak annual mean warming at high latitudes and cooling across the tropics and subtropics notable in both the *lig127k* and *midHolocene*. This pattern is suggestive of the obliquity-driven changes to the annual mean insolation which brings about a weak increase of up to  $4 \text{ W m}^{-2}$  at high latitudes in both, and a decrease of about  $1 \text{ W m}^{-2}$  in *midHolocene* (about  $0.5 \text{ W m}^{-2}$  in *lig127k*) in the tropics. Interestingly, the increase in obliquity is larger in *midHolocene* than in *lig127k*, yielding slightly greater annual mean insolation anomalies, yet the annual mean surface temperature anomalies are weaker in the *midHolocene* in comparison, especially over the high northern latitudes. Also, the *midHolocene* has a greater decrease in greenhouse gas

**Table 2**

Summary of Climatic Variables in the midHolocene, lig127k, and piControl Simulations. Means are Computed Over the Final 100 Years of Each Integration. Niño3.4 Statistics are Computed Over the Last 200 Years of Monthly Time Series with Mean Annual Cycle and Trend Removed and Represent the Min/Mean/Max of 30-yr Running Means. Output has Been Transformed to the Celestial Calendar

	piControl	midHolocene	lig127k
Top-of-atmosphere energy imbalance (W m <sup>-2</sup> )	0.017	0.061	0.060
Global surface temperature (TS, °C)			
JJA	16.87	16.92	17.96
DJF	13.51	13.15	12.50
Annual	15.25	15.06	15.15
NH (20-90 N) JJA land surface temperature (TS, °C)	20.40	21.88	24.83
Global annual precipitation (mm day <sup>-1</sup> )	2.95	2.93	2.93
Tropical (20S-20N) JJA land precipitation (mm day <sup>-1</sup> )	3.66	3.94	4.65
Niño3.4 std dev (°C)	0.96/1.12/1.29	0.82/1.03/1.25	0.70/0.89/1.10
Transports (Sv)			
Drake Passage	146.55	132.99	124.59
Florida Strait	25.57	25.10	25.03
AMOC (Sv) (Total)			
NH Max (lat > 25 N, z > 500 m)	23.71	24.86	25.28
Max@34S	17.60	18.10	18.45
NH Min (lat > 25 N, z > 500 m)	-2.26	-2.58	-2.97
Min@34S, z > 500 m)	-1.99	-1.92	-2.01
Atlantic Ocean NHTmax (PW)_	1.06	1.09	1.12
Sea ice area (106 km <sup>2</sup> )			
NH - annual	11.2	10.8	10.1
NH - minimum	5.9	4.0	1.6
SH - annual	10.6	10.4	10.2
SH - minimum	2.8	2.4	3.3

forcing than *lig127k*. This suggests other processes remain important in driving the resulting changes to the annual mean surface temperature such as ocean and cryosphere memory. Arctic surface ocean gains heat in response to sea ice loss in summer due to the greater open ocean, and due to higher ocean heat capacity (memory), the warmer ocean surface temperatures are retained into the fall and winter seasons, resulting in thinner winter sea ice. The thinner winter sea ice is consistent with a weaker insulating effect of sea ice, allowing increased air-sea heat exchange and hence increased winter air temperatures (Serreze & Barry, 2011).

#### 4.1.2. Precipitation

The numerous improvements incorporated into the atmospheric component of CESM2 have had a positive impact on the simulation of precipitation, including reductions in the biases of the Intertropical Convergence Zone (ITCZ), over the tropical oceans, and the Amazon, Australia, and western U.S. regions (Danabasoglu et al., 2020). The seasonal and latitudinal structure of insolation anomalies at 6 ka and 127 ka promote enhanced NH monsoons and reduced SH monsoons in the *midHolocene* and *lig127k* simulations (Figure 4), with little change in annual mean, global precipitation (Table 2). Over North Africa, JJA precipitation increases and extends northward into the Sahara as well as southward in central Africa as compared to the *piControl*, with these changes greater in the *lig127k* than the *midHolocene*. The Asian monsoon is enhanced in both interglacial simulations as compared to the *piControl*, with again greater increases in precipitation in the *lig127k* simulation than the *midHolocene* simulation. The *lig127k* simulation shows a band of enhanced JJA precipitation over the islands of Malaysia, Indonesia, and Papua New Guinea, also present in the *midHolocene* simulation but not statistically significant. Overall tropical (20°S-20°N) land, JJA precipitation increases by 8% in the *midHolocene* and 27% in the *lig127k* as compared to the *piControl*.

The SH monsoons and associated austral summer precipitation over southern Africa, Australia, and South America are reduced in both interglacial simulations as compared to the *piControl*, with greater decreases in precipitation in the *lig127k* than the *midHolocene*.

Over the oceans, increased precipitation is associated with the winter (DJF) mid-latitude storm tracks over the North Pacific and North Atlantic Oceans compared to the *piControl*, most prominently in the *lig127k* but

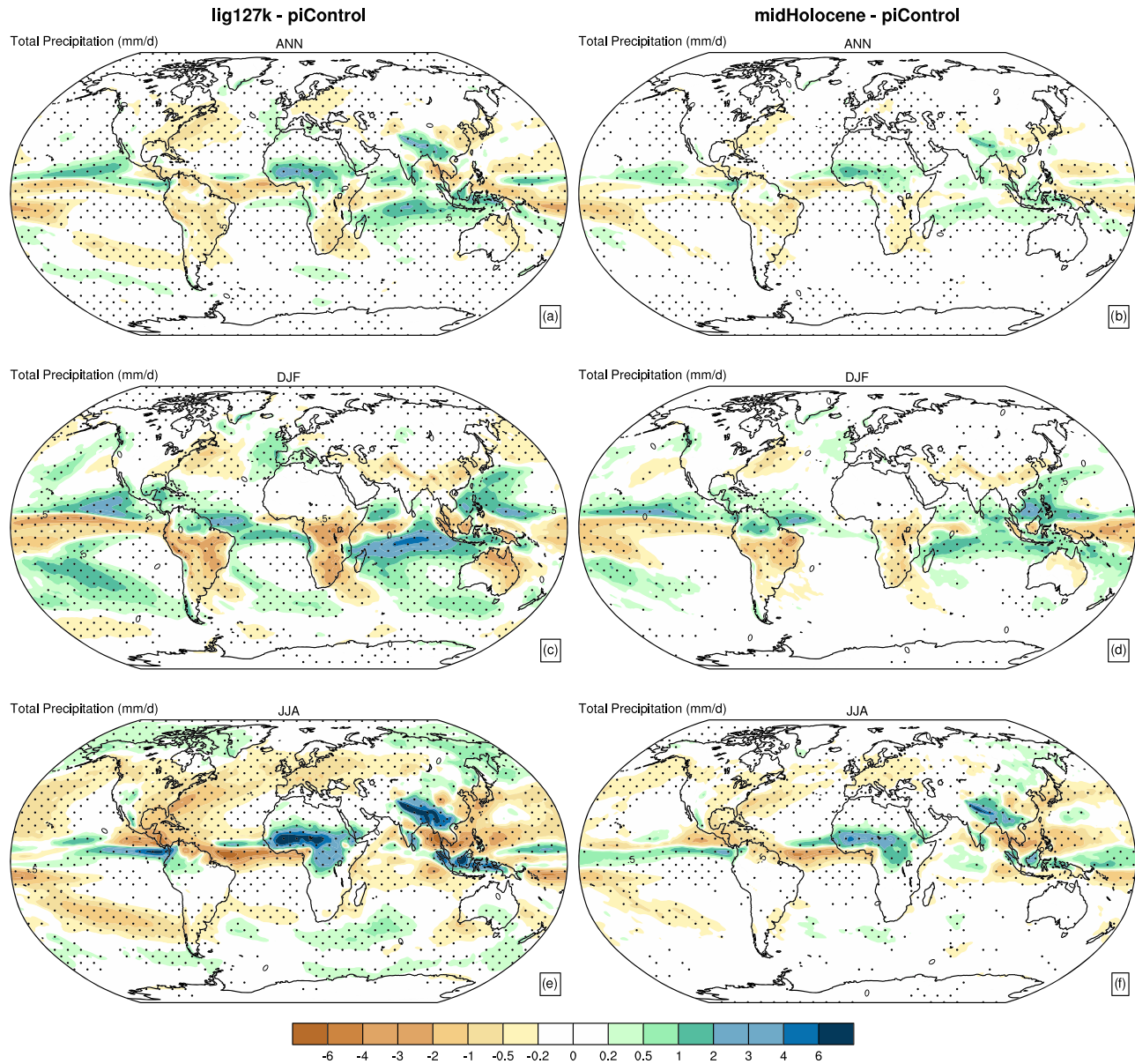


**Figure 4.** Annual and seasonal precipitation anomalies (mm/day) in the *lig127k* and *midHolocene* simulations as compared to the *piControl* simulation. Stippling indicates anomalies statistically significant at 95%.

also in the *midHolocene*, and decreased precipitation associated with the winter (JJA) mid-latitude storm tracks over the South Pacific, South Atlantic, and southern Indian Oceans compared to the *piControl* (Figure 4). Annually, the ITCZ over the tropical oceans shifts northward with the interglacial forcings.

#### 4.1.3. Dust Aerosol Optical Depths

As explained in Section 3, the *midHolocene* and *lig127k* simulations share the same soil erodibility map for dust (Otto-Bliesner et al., 2017). In this section we focus on the Holocene, for which observational constraints on the dust cycle are available (Albani et al., 2015). Simulated dust deposition (wet + dry) for the *midHolocene* captures fairly well the observational constraints represented by dust mass accumulation rates from paleodust archives integrated for the 6 ka time slice (5–7 ka) (Figure 5(a); Albani et al., 2015).

Dust Aerosol Optical Depth (AOD) anomalies between *midHolocene* and *piControl* show a significant reduction in the North African dust plume over the continent that extends into the Atlantic Ocean (Figure 5(b)). In terms of global budgets, total dust deposition (or emissions) amounts to  $2,200 \text{ Tg yr}^{-1}$  for the *piControl*

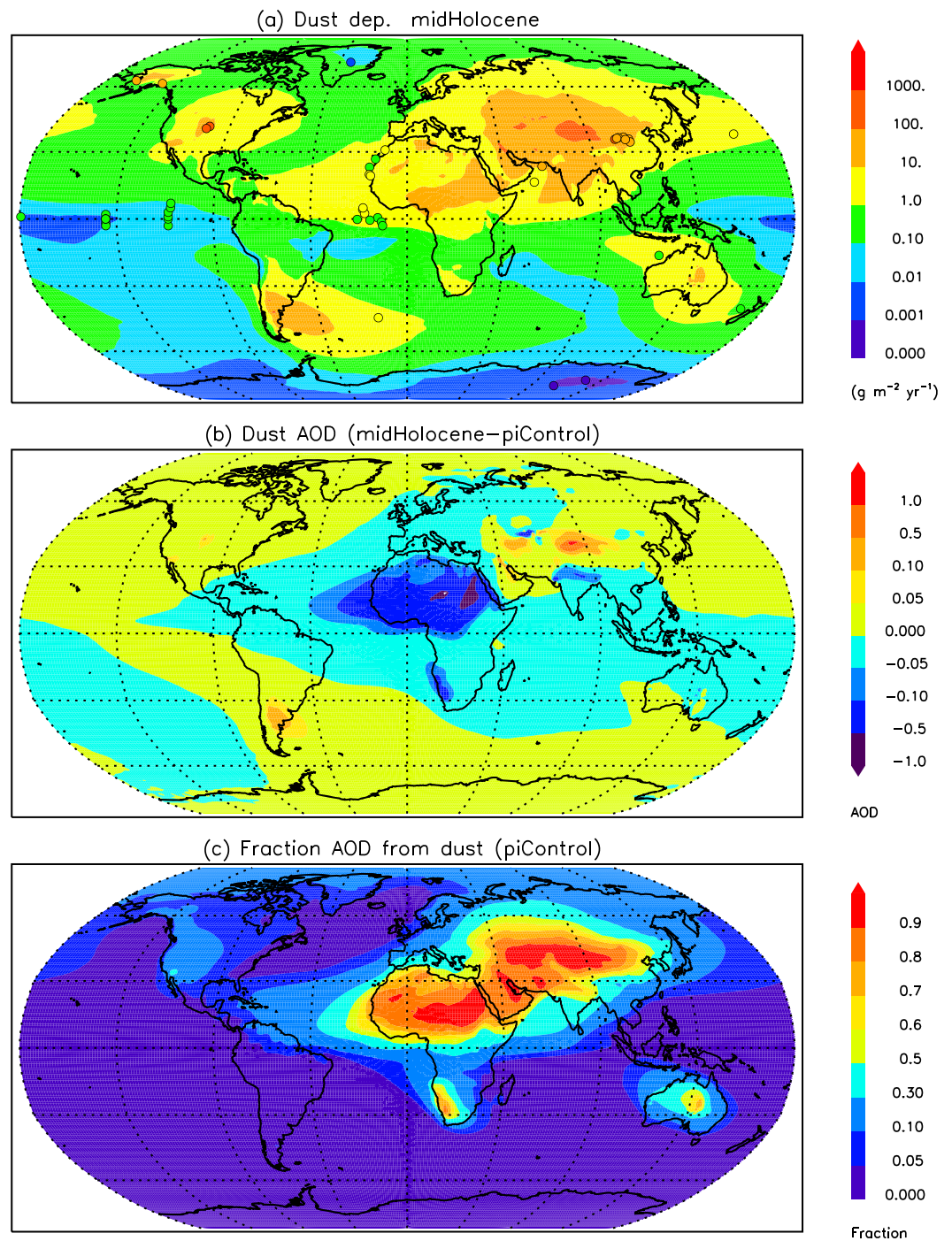


**Figure 5.** Dust in the *midHolocene* and *piControl* simulations. a) Comparison of simulated total (wet + dry) dust deposition (contours) against observational constraints from paleodust archives (circles) for the *midHolocene* (Albani et al., 2015), using the same color scale. b) Difference in simulated dust aerosol optical depth between the *midHolocene* and *piControl* cases. c) Fraction of aerosol optical depth due to dust with respect to all-aerosols, in the *piControl* simulation.

and 1,824 Tg yr<sup>-1</sup> for the *midHolocene* cases, respectively. Compared with previous estimates using an older version of the CESM model (Albani et al., 2016), we have lower emissions in both climates and a more accentuated (17% vs 9%) decrease in dust emissions between *midHolocene* and *piControl*.

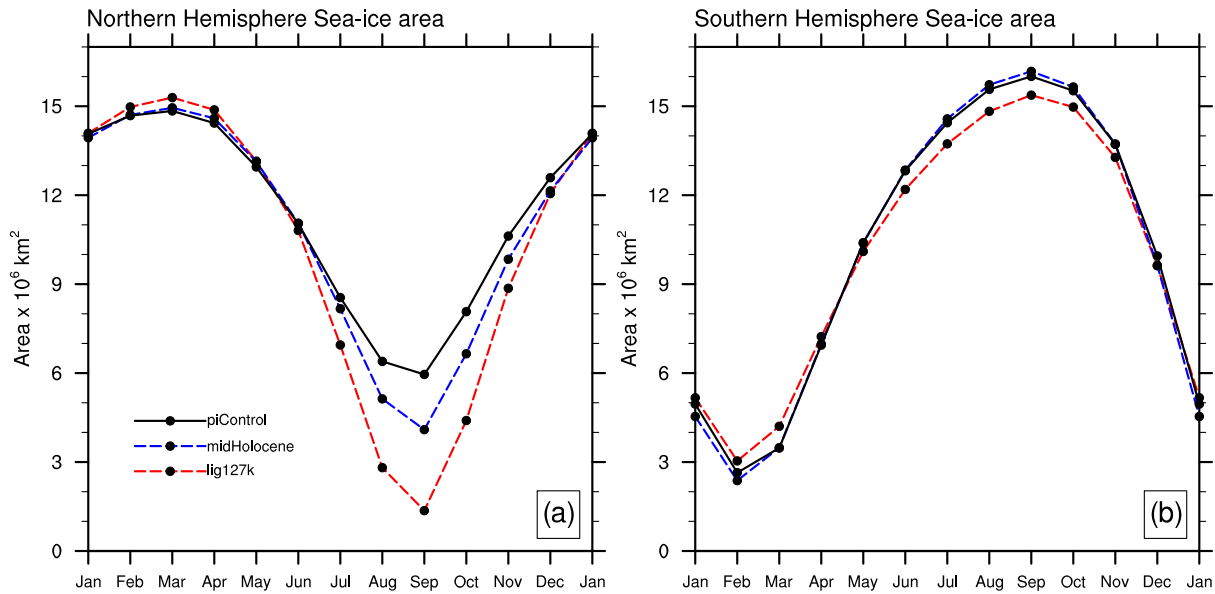


**Figure 6.** The annual cycle of sea ice area ( $10^6 \text{ km}^2$ ). Defined as the areal integral of sea ice fraction multiplied by the grid cell area. a) Northern Hemisphere and b) Southern Hemisphere in the *piControl*, *midHolocene*, and *lig127k* simulations.

At the same time, in our simulations with CESM2, dust AOD was reduced from 0.030 in *piControl* to 0.022 in the *midHolocene* case, accounting for 19% and 25% of the total AOD, respectively. In particular, we note how dust dominates AOD over the entire arid belt extending from North Africa to East Asia (Figure 5(c)). In the absence of more specific diagnostic variables for dust, AOD gives a first-order idea of the potential importance of dust changes in mediating Direct Radiative Effects (DRE). We should note that dust interacts not only with solar radiation, but also with thermal radiation.

## 4.2. Sea Ice and Ice Sheets

### 4.2.1. Northern and Southern Hemisphere Sea Ice

The annual cycles of NH sea ice area show reduced areal coverage during boreal summer, but little change during boreal winter, in both the *midHolocene* and *lig127k* simulations as compared to the *piControl* (Figure 6(a)). The September minimum is 33% less in the *midHolocene* and 75% less in the *lig127k*. NH sea ice area remains below that of the *piControl* from July to November in both the *midHolocene* and *lig127k* simulations. It should be noted that the *piControl* has a thin ice bias in CESM2(CAM6) from more melting during the boreal summer months resulting in a low summer ice area as compared to satellite observations (Danabasoglu et al., 2020).

The location of the climatological mean Arctic sea-ice edge in August–September (AS) denoted by the extent (fractional ice area >15%) retreats from the *piControl* to the *midHolocene* to the *lig127k* (Figure S2). This corresponds to the markedly thinner sea ice across the NH polar region in both the *midHolocene* and *lig127k* in comparison to the *piControl* consistent with the enhanced seasonal cycle of insolation in the NH. Negative AS sea ice thickness anomalies in the central Arctic exceed  $\sim 0.5 \text{ m}$  in the *midHolocene* and  $\sim 1 \text{ m}$  in the *lig127k* with greater thinning found towards Greenland and the North American coast in both simulations.

The *midHolocene* annual cycle of SH sea ice area shows little change from the *piControl* (Figure 6(b)). The *lig127k* has a dampening of seasonal cycle of SH sea ice area with somewhat more area in austral summer and less area in austral winter than the *piControl*. The climatological mean February–March (FM) sea ice extent (fractional ice area >15%) is also roughly similar in the SH in all simulations, except for a somewhat greater equatorward extent in the Pacific sector of the Southern Ocean in the *lig127k* in FM (Figure S2). The simulated responses of climatological mean FM sea ice thickness are rather weak in the SH in comparison to the response found in the NH however. The *lig127k* has a somewhat thicker sea ice distribution in the Pacific

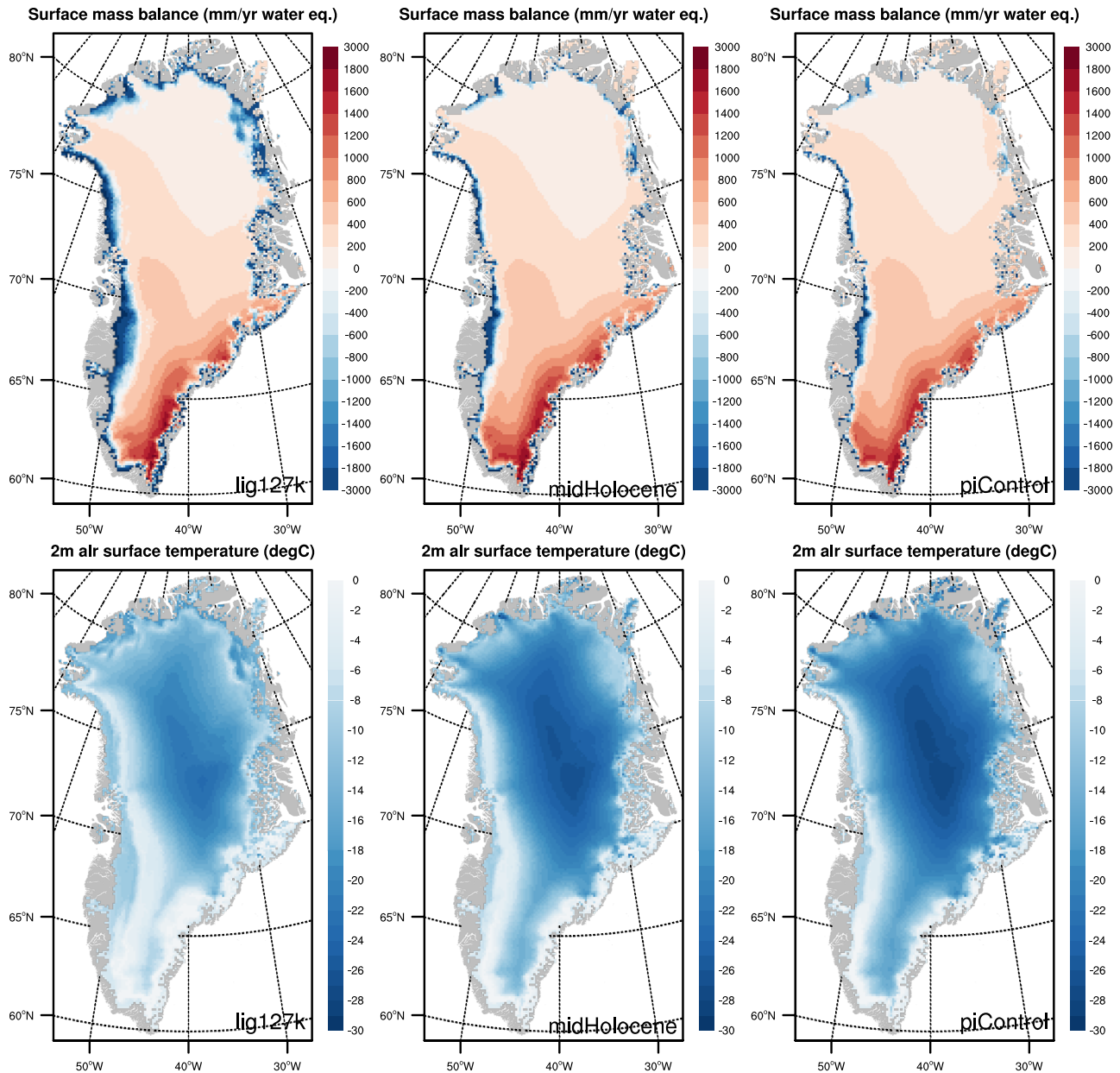


**Figure 7.** Surface mass balance (mm water equivalent/yr) and surface air temperature (°C) of the Greenland ice sheet in the *lig127k*, *midHolocene*, and *piControl* simulations. The CESM2.1 results are downscaled using the CLM multiple elevation classes to the 4-km CISM grid.

sector of the Southern Ocean, with thinning mostly elsewhere, except east of the Antarctic Peninsula. The *midHolocene* shows a greater thinning response in the Weddell Sea in comparison to the response found in the *lig127k* simulation.

#### 4.2.2. Greenland Ice Sheet

The Greenland ice sheet Surface Mass Balance (SMB) for the 1961–1990 mean of the CESM2(CAM6) historical simulation agrees well with the regional atmospheric climate model RACMO2 simulation, albeit with a positive SMB bias in southern Greenland associated with excessive snowfall (Danabasoglu et al., 2020; van Kampenhout et al., 2020). Associated with warmer climates of the LIG and MH, enhanced precipitation with storm tracks results in more positive SMB in southern and southeastern Greenland, particularly so in the *lig127k*, as compared to the *piControl* (Figure 7). Areas of negative SMB (more ablation than accumulation annually) expand along edges of the Greenland ice sheet, particularly in western Greenland and also

northwest Greenland, in the *midHolocene* and *lig127k* simulations. At high elevations in central Greenland, the small, positive SMB in the *piControl* remains unchanged in the *midHolocene* and *lig127k*. Annual temperatures are warmer in the *midHolocene* and *lig127k* simulations but remain below freezing year-round. The extent of negative SMB is especially pronounced in the *lig127k* simulation, suggesting the Greenland ice sheet would lose mass and contribute to the average global mean sea level rise if CESM2 was coupled to CISM2 dynamically.

### 4.3. Ocean

#### 4.3.1. Barotropic Streamfunction

The interglacial simulations show changes in the annual mean barotropic transport streamfunction. Globally the largest differences in the barotropic ocean transport compared to the *piControl* are found in the Southern Ocean and the North Atlantic (Figure 8). In the Southern Ocean, the Antarctic Circumpolar Current (ACC) weakens in both interglacials, but to a greater degree in *lig127k* as compared to *midHolocene*. The transport through the Drake Passage is reduced by  $\sim 22.0$  Sv in the *lig127k* and  $\sim 13.6$  Sv in the *midHolocene* (Table 2). In addition, the dipole pattern in the annual mean barotropic transport anomalies in the Pacific sector of the Southern Ocean suggests a modest strengthening of the barotropic transport within the South Pacific subtropical gyre and the ACC at the equatorward edge in comparison to the *piControl*. This dipole pattern is similar but weaker in *midHolocene* as compared to *lig127k*. The response of ACC is consistent with a small shift northward of the southern westerlies in the Pacific sector, resulting in a weakening of the zonal wind stress at the latitude of the Drake Passage (not shown).

In the North Atlantic (Figure 8), the annual mean barotropic streamfunction associated with the circulation within the subtropical gyre system strengthens in both orbitally driven cases relative to the *piControl*, with a greater strengthening found in the *lig127k*. The strengthening occurs north of the Florida Straits, and equatorward of  $\sim 38^\circ\text{N}$ , with a decrease in the barotropic streamfunction found at the northern edge of the subtropical gyre. In the subpolar North Atlantic, both orbitally driven cases show an increase in the cyclonic circulation of the subpolar gyre, with the *lig127k* exhibiting a greater anomaly. These anomalies in the barotropic streamfunction in the North Atlantic are consistent with a strengthening of the westerlies over the N. Atlantic, which increases the magnitude of the wind stress curl in the vicinity of the subpolar gyre and western boundary of the subtropical gyre.

#### 4.3.2. Meridional Overturning Circulation and Deep Vertical Mixing

The Atlantic meridional overturning circulation (AMOC) appears to be weakly sensitive to changes in the combined forcing from the seasonal and latitudinal redistribution of insolation and the small decrease in atmospheric greenhouse gases (Figure 9, Table 2). A weak increase in the strength of the meridional overturning circulation cell associated with the formation of the model North Atlantic Deep Water (NADW) is found north of  $\sim 30^\circ\text{N}$  in the upper thermocline and is reflected in the weak increase in the maximum AMOC (Table 2). In comparison to the *piControl* simulation, both paleoclimate simulations exhibit a weak increase in the northward circulation of southern-sourced bottom water in the deepest levels of the Atlantic basin (Table 2, Figure 9). The *piControl* shows a somewhat weaker circulation of Antarctic Bottom Water (AABW) than reported for the 1990–2014 period in the historical simulation in Danabasoglu et al. (2020).

The deepest late winter mixing takes place in the North Atlantic in association with the formation of model NADW. In association with the increase in AMOC is a change in the late winter deep vertical mixing in the subpolar gyre region. In the *midHolocene* and *lig127k* simulations, late winter deep vertical mixing decreases somewhat (by  $\sim 150$  m) in the mouth of the Labrador Sea, where deep later winter mixing reaches depths of  $\sim 1,600$  m in *piControl*, and intensifies greatly by  $\sim 500$  m deeper off the east coast of Greenland and directly south of Greenland within the subpolar gyre (Figure S3). In the Nordic Seas south of Spitzbergen (Figure S3) the late winter mixing decreases in *lig127k* and *midHolocene*. The pattern of mixed layer depth anomalies relative to the *piControl* is similar in both but more amplified in the *lig127k* compared to the *midHolocene*.

In the SH, the late winter vertical mixed layer depths associated with the formation of relatively fresh and cold Antarctic Intermediate Water, extending west and east of the southernmost tip of South America, increase in the *midHolocene* and *lig127k*, with larger increases found in the *lig127k* (Figure S3). A modest reduction in the late winter mixed layer depth is noted however, over the band of relatively well mixed upper water associated with the lighter type of intermediate mode water, known as the Subantarctic Mode Water, which extends west from the western Pacific into the Indian Ocean.

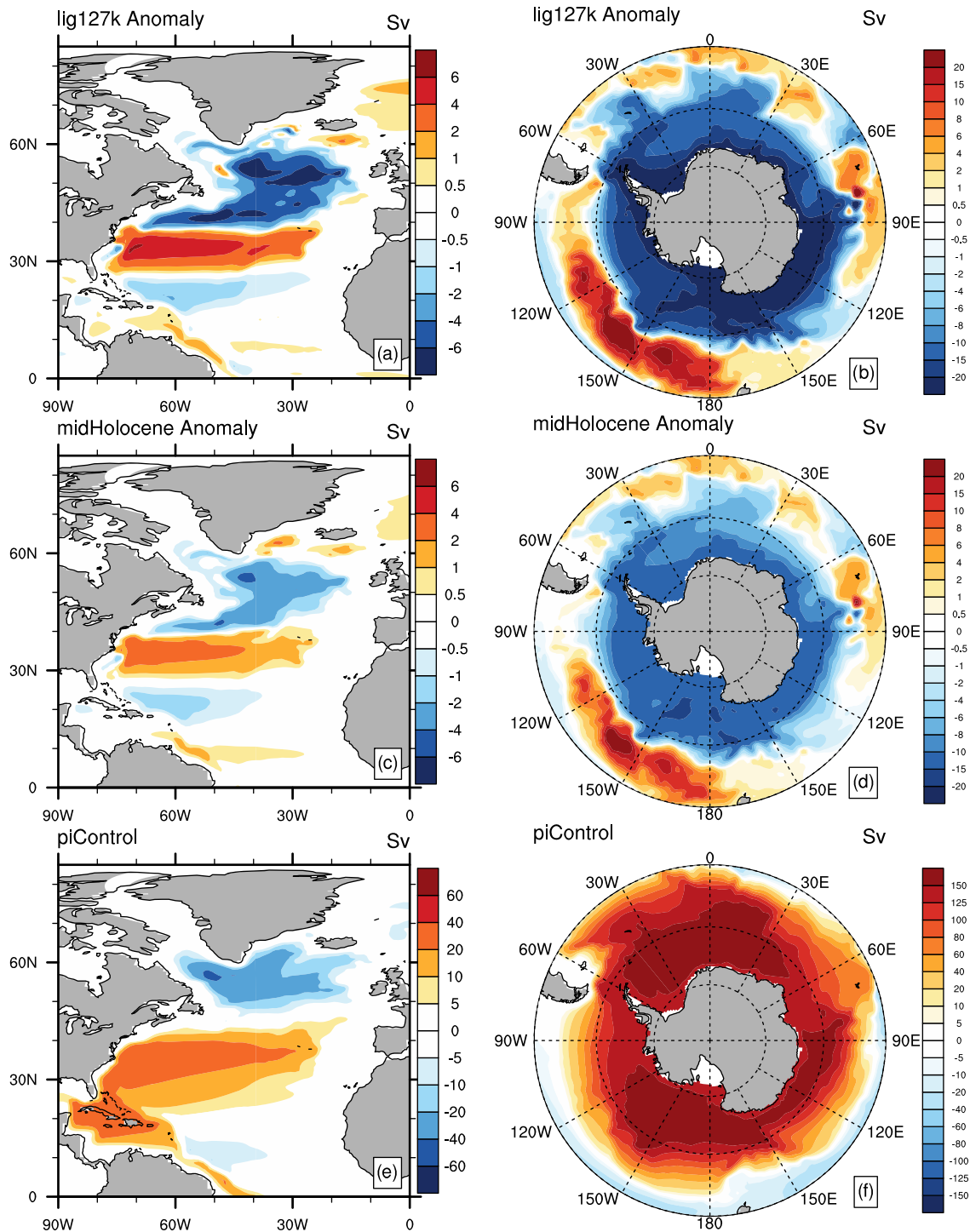


**Figure 8.** Anomalies of annual mean barotropic streamfunction (BSF) for the *lig127k* (top), *midHolocene* (middle) as compared to the mean BSF in the *piControl* (bottom) simulations for the North Atlantic (left) and the Southern Ocean (right) basins. Positive (negative) streamlines denote clockwise (counterclockwise) circulation and anomalies, such that anomalies of the same (opposite) sign as the *piControl* BSF suggest strengthened (weakened) circulation. Note the change in contour interval between upper and lower, and left and right panels.

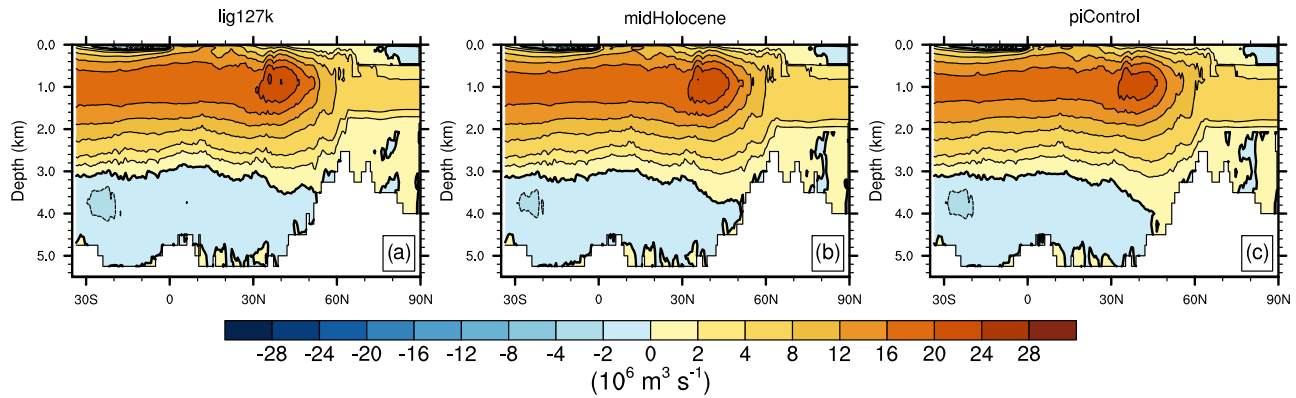


**Figure 9.** Total (Eulerian plus eddy-induced components) Atlantic Ocean (and contiguous northern bays and seas) mean meridional overturning circulations (Sv,  $1 \text{ Sv} = 10^6 \text{ m}^3 \text{ s}^{-1}$ ) in the a) *lig127k*, b) *midHolocene*, and c) *piControl* simulations. The positive and negative contours indicate clockwise and counterclockwise circulations, respectively.

#### 4.3.3. Tropical Seasonal Cycle of Sea Surface Temperature (SST) and El Niño - Southern Oscillation (ENSO)

Improvements in ENSO characteristics (period, amplitude, seasonal cycle) in CCSM4 as compared to CCSM3 are retained in CESM2 (Danabasoglu et al., 2020). Comparable to observations, the Niño3.4 SST index in the *piControl* simulation has maximum power at periods of 3–7 years, though with the Niño3.4 SST standard deviation overestimated by ~30% (Figure 10(f)). The annual cycle of the monthly standard deviation peaks in November–December–January with a minimum in June–July (Figure 10(e)). The Niño3.4 index has reduced power going from the *piControl* to *midHolocene* to *lig127k*, with a 20% reduction in the Niño3.4 standard deviation in the *lig127k* as compared to the *piControl* (Table 2). The *lig127k* also exhibits a much flatter annual cycle of monthly standard deviations with the minimum shifted to August–September (Figure 10(a)).

The seasonal cycle of SST along the equator in the Pacific shows a strong sensitivity to the orbitally-driven changes in the seasonal cycle of insolation in the tropics (Figure S4). The anomalies in the seasonal cycle are largest in the eastern to central Pacific where the equatorial thermocline is shallow and coupled ocean–atmosphere dynamics play an important role in the annual cycle of equatorial SST, and more muted west of the dateline where the thermocline is deep. The anomalies in the annual SST cycle with respect to the *piControl* are the same order of magnitude as the amplitude of the annual cycle. The anomalies in the seasonal cycle of SST along the equator in the central and eastern Pacific with respect to the *piControl*, are generally in phase with the tropical insolation anomalies as shown in Figure 1. Relative to the seasonal cycle in the *piControl* in both paleoclimate simulations, central to eastern Pacific seasonal warm anomalies are largest when the insolation anomalies are most positive (i.e., JJA for *lig127k* and JAS for *midHolocene*) and the greatest cooling relative to the *piControl*'s seasonal cycle occurs when insolation anomalies are most negative (i.e., JFM for the *midHolocene* and DJF for *lig127k*).

The eastern Pacific seasonal warming in *lig127k* relative to the annual mean (Figure S4) is shifted later by a few months in phasing and warms with greater amplitude than the *piControl*. The large negative insolation anomalies during the late boreal winter/early spring in *lig127k* tend to mute the start of the warming in the eastern equatorial Pacific, then the seasonal equatorial warming is enhanced by the large positive insolation anomalies starting in late spring and peaking in boreal summer. This tendency shifts the peak seasonal warming by a couple of months. The equatorial insolation anomalies are weaker and shifted later in *midHolocene* than in *lig127k*. The negative insolation anomaly in *midHolocene* peaks in early boreal spring, muting the spring warming, while the positive insolation anomaly starts later and extends into the boreal fall, muting the cooling tendency by strong equatorial upwelling. The *lig127k* shows greater cooling from November to March in comparison to the *piControl* and the *midHolocene* when the large negative *lig127k* insolation anomalies tend to enhance the tendency of seasonal cooling by equatorial upwelling.

In the central and eastern Pacific, the amplitude of the seasonal cycle of SST in the *lig127k* is larger than in the *piControl*, whereas the seasonal SST amplitude is noticeably weaker in the *midHolocene*, particularly

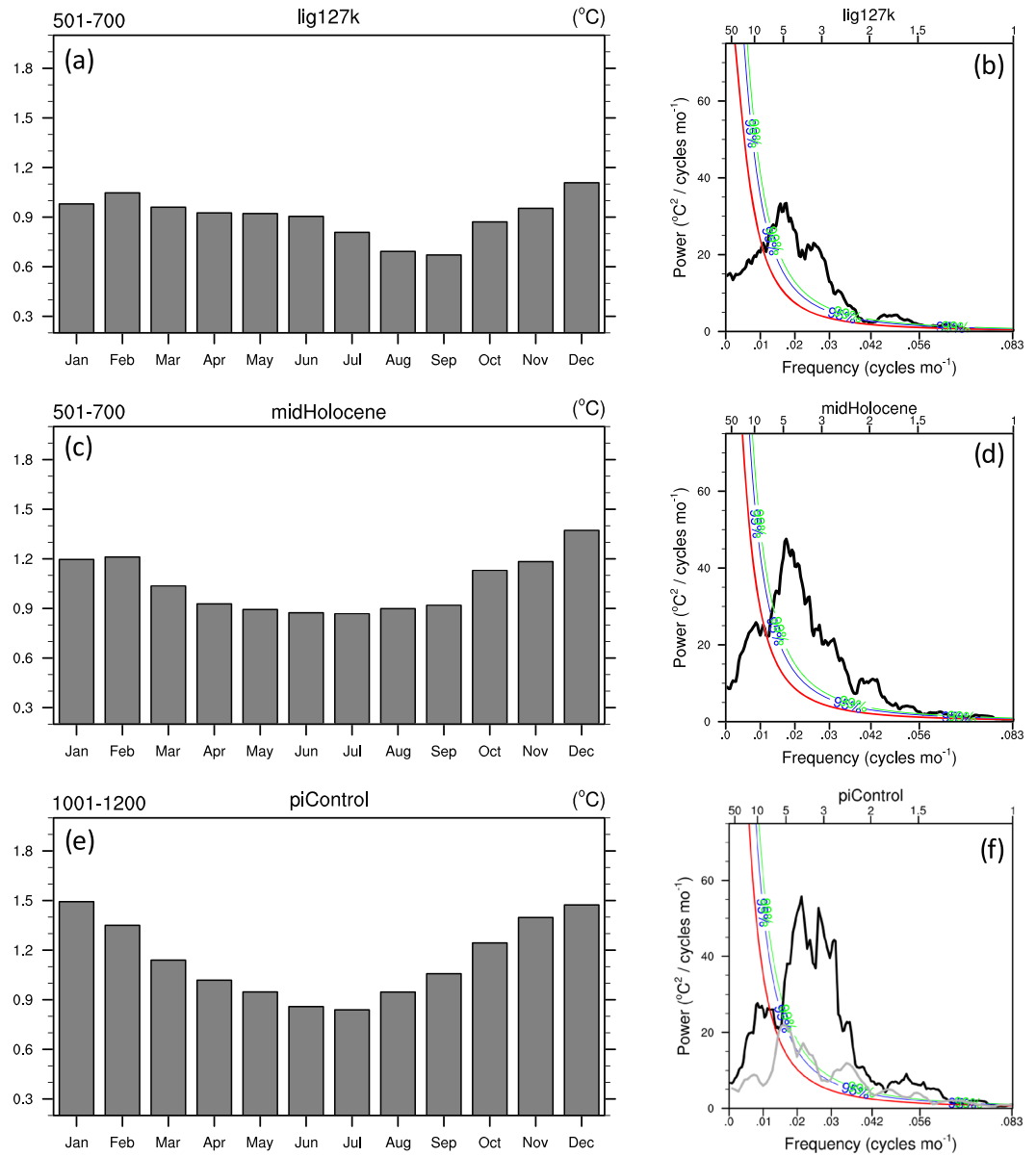


**Figure 10.** The monthly standard deviations (°C) and power spectra (°C<sup>2</sup>/cycles mo<sup>-1</sup>) of Niño3.4 SST in the *lig127k*, *midHolocene*, and *piControl* simulations. The mean annual cycle is removed prior to every calculation by subtracting the long-term monthly means. The best-fit first-order Markov red noise spectrum (red curve) and its 95% (blue curve) and 99% (green curve) confidence bounds are shown for the power spectra. The observed power spectra for 1920–2018 from the HadISST dataset is shown in light gray in panel f).

along the eastern boundary of South America, and in the amplitude of seasonal cooling in boreal fall. By itself, the opposite responses of the magnitude of the seasonal cycle do not appear to explain the weaker ENSO amplitude in both paleoclimate simulations as compared to the *piControl*. Rather, the colder annual mean SST compared to the *piControl*, in addition to colder tropical SSTs in the boreal cold season, may act to moderate the amplitude of the ENSO events which tend to peak at the end of the year.

## 5. Model-Model and Model-Data Comparisons

To inform our understanding of the climate responses to the orbital forcing at 6 ka and 127 ka, comparing the CESM2 *midHolocene* and *lig127k* results to the latest proxy reconstructions is instructive. Also, model differences are considerable between the older versions of the models (CCSM3 and CCSM4) and CESM2,

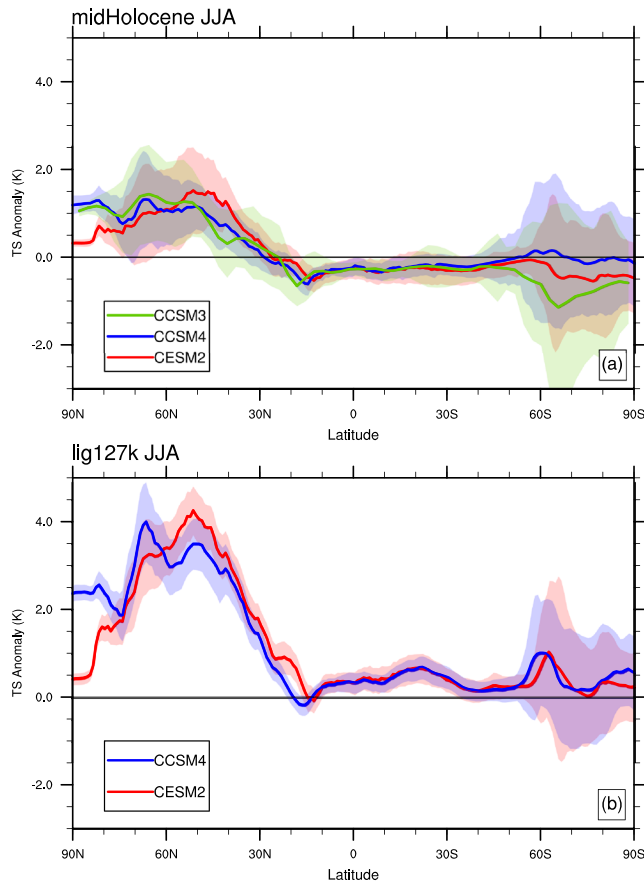


**Figure 11.** Zonal-average surface temperature anomalies ( $^{\circ}\text{C}$ ) through multiple versions of CESM. a) JJA changes from preindustrial for 6 ka (CCSM3, CCSM4, and CESM2); b) JJA changes from preindustrial for 127 ka (CCSM4 and CESM2). Shading represents the 2-standard error.

and the *midHolocene* simulation. These include east–west patterns of positive/negative 6 ka surface air temperature anomalies as compared to PI in eastern/western U.S., eastern China/Tibet, and western/eastern North Atlantic. CESM2 and the proxy reconstruction also indicate warmer surface temperatures over South Africa and Brazil at 6 ka as compared to PI. CESM2 simulates no change in annual temperatures at the locations of the East Antarctica ice cores in agreement with the 6 ka reconstruction, but also no change at the locations of the Greenland summit ice cores where the reconstruction suggests modest positive surface temperature anomalies at 6 ka. Over Europe and Canada, the temperature proxies indicate substantial warming nearby to substantial cooling making a credible model-data comparison difficult. Similarly, over North Africa, the only one record available does not allow an assessment on whether the simulated annual cooling is reasonable. The latter is consistent with the enhanced monsoon precipitation and cloud cover simulated in the *midHolocene* simulation.

Much less data are available to compare to the *lig127k* simulation of annual surface temperatures (see Otto-Bliesner et al., 2020 for discussion and tables of reconstructions). Similar east–west contrasts of simulated temperature anomalies over the U. S, China, and the North Atlantic seen in the *midHolocene* simulation are also present in the *lig127k* simulation (Figure 12(b)). As well, the *lig127k* has positive surface temperature anomalies over South Africa and Brazil that cannot yet be verified from proxy records. Over Europe, the temperature proxies show a generally consistent picture of annual warming in the *lig127k* simulation. The polar ice cores and the *lig127k* simulation suggest higher surface temperature at 127 ka than PI, though CESM2 underestimates this warming. Note that the protocol for the *lig127k* simulation adopts modern ice sheet extents and elevations for the Greenland and Antarctic ice sheets. The proxy-reconstructed

which are associated with significant improvements made in the physics of the component models. Simulations with these three versions were conducted using the nominal  $1^{\circ}$  resolution displaced pole grid for sea ice and ocean components and either the FV0.9x1.25 horizontal grid in the atmospheric component (CESM2 and CCSM4) or the T42 ( $\sim 2.8^{\circ}$  resolution) grid in the CCSM3. CCSM4 was used in CMIP5 and PMIP3, whereas CCSM3 was used in PMIP2. Though there were small variations between the different PMIP and CMIP experimental protocols, the differences are not large enough to explain major differences between the three model versions for a given experiment.

### 5.1. Temperature

The JJA zonal-average surface temperature anomalies are compared for the three versions of the model (Figure 11). For the *midHolocene*, the JJA zonal-average surface temperature anomalies from  $\sim 40^{\circ}\text{S}$  to  $\sim 20^{\circ}\text{N}$  are negative and of similar magnitude across the three model versions. All have maximum warming in the NH mid-latitudes of approximately  $1^{\circ}\text{C}$ . Differences in the surface temperature anomalies at polar latitudes in both hemispheres are related to simulation of sea ice thickness and extent in the respective preindustrial simulations, as discussed in Section 5.4.

Notable for the *lig127k* simulations are that the JJA zonal-average surface temperature anomalies are positive at all latitudes except  $\sim 25^{\circ}\text{N}$  in CCSM4 and CESM2. These positive anomalies peak also similarly at  $3\text{--}4^{\circ}\text{C}$  in the NH mid-latitudes. As for the MH, differences in the surface temperature anomalies at polar latitudes in both hemispheres are related to simulation of sea ice thickness and extent in the respective preindustrial simulations.

The CESM2 *midHolocene* annual surface air temperature anomalies can be compared to the 6 ka paleo-temperature records from a new global compilation of quality-controlled, published, temperature-sensitive proxy records for the Holocene (Figure 12(a)) (Kaufman et al., 2020). Several regional features are in general agreement between the proxy records

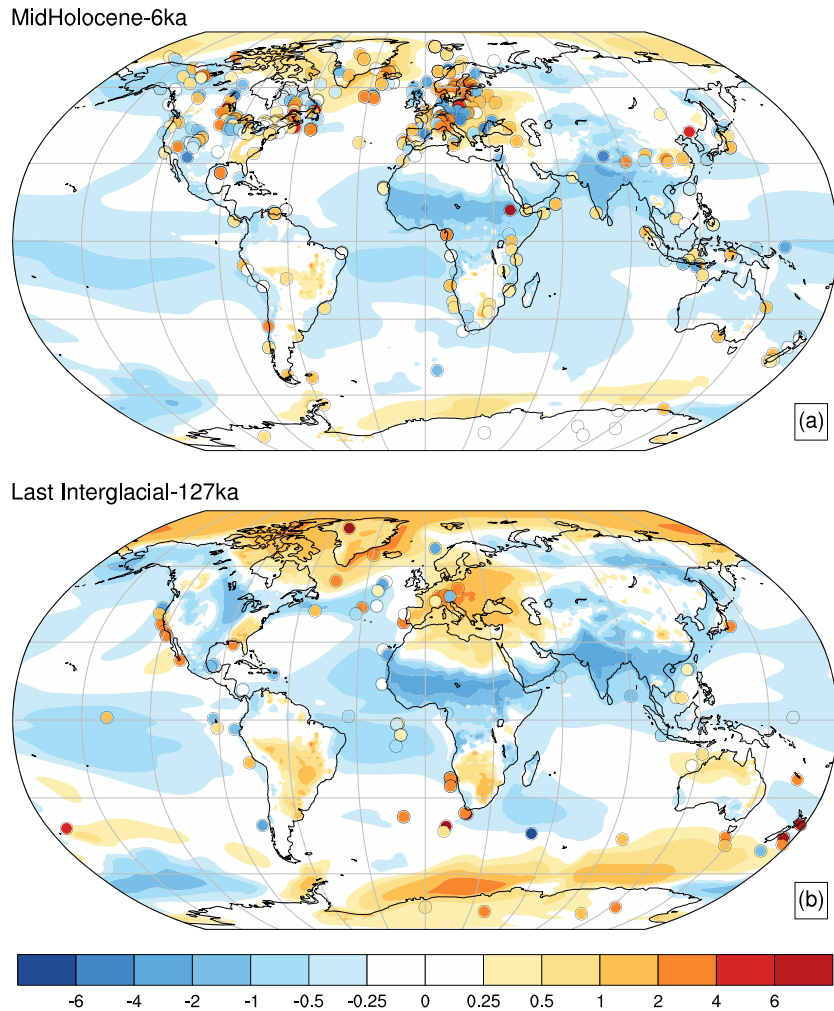


**Figure 12.** Annual surface air temperature anomalies ( $^{\circ}\text{C}$ ) in the *lig127k* and *midHolocene* simulations as compared to proxy reconstructions. See Kaufman et al. (2020) and Otto-Bliesner et al. (2020) for details of proxy reconstructions.

positive surface temperature anomalies in the coastal upwelling regions off California, as expected are not seen in the *lig127k* simulation. Models such as CESM2 do not have high enough resolution to realistically simulate coastal upwelling.

The 6 ka proxy reconstruction indicates only modest changes in surface temperatures during the boreal summer over North America, Nordic Seas, Europe, western Eurasia and far northern Africa in regions where the *midHolocene* simulation predicts warmer surface temperatures (Figure 13(a), 13(c)). It should be noted that the lack of spatial coherence in the European temperature reconstructions complicates comparisons with the CESM2 outputs. Both time periods show patterns of greater summer warming over the NH continents than the North Atlantic, but the *lig127k* simulation has significantly greater positive surface temperature anomalies. Notable, is the good agreement of the simulated and proxy records over Baffin Island and the central North Atlantic for 127 ka (Figure 13(b)). On the other hand, proxy records south of Greenland and in the Nordic Seas indicate colder SSTs at 127 ka than PI (Figure 13(d)). This model-data mismatch could be associated with meltwater from potentially remnant ice sheets over Canada and Scandinavia (Barlow et al., 2018), which the *lig127k* simulation did not incorporate.

## 5.2. Precipitation

All three model versions (CCSM3, CCSM4, CESM2) successfully capture the large-scale observed modern features of precipitation over North Africa, with annual precipitation peaking at equatorial latitudes and

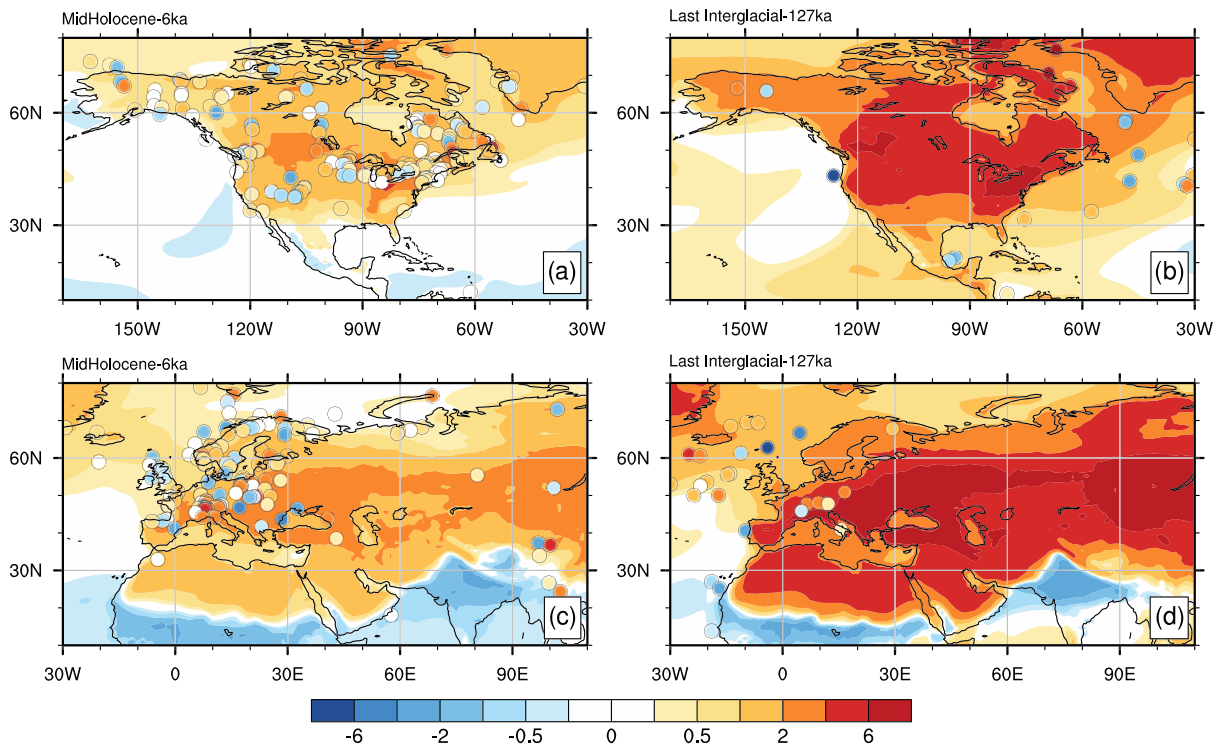


**Figure 13.** JJA surface air temperature anomalies ( $^{\circ}\text{C}$ ) in the *lig127k* (right) and *midHolocene* (left) simulations as compared to proxy reconstructions. See Kaufman et al. (2020) and Otto-Bliesner et al. (2020) for details of proxy reconstructions.

becoming negligible north of  $20^{\circ}\text{N}$  (Figure S5). Although the maximum precipitation in the equatorial regions is reduced in CESM2 from that simulated by CCSM3 and CCSM4, all three versions still overestimate annual precipitation south of  $10^{\circ}\text{N}$ . The summer monsoon over North Africa intensifies and shifts northward in the three model versions, though, not sufficient to explain the proxy reconstruction. This is also true for all comparable simulations in PMIP3 and PMIP4 for the *midHolocene* (Brierley et al., 2020), highlighting a shortcoming of current models in simulating the African Humid climate. The CESM2 *midHolocene* simulation has less northward extent of the monsoon than the comparable simulations in earlier versions of the model. As also noted in the multi-model ensembles (Otto-Bliesner et al., 2020) and consistent with proxy reconstructions (Scussolini et al., 2019), the areal extents and total water precipitated for the North African monsoon are enhanced in the 127 ka simulations in CCSM4 and CESM2 as compared to their corresponding simulations at 6 ka.

It should be noted that none of the three model versions include interactive vegetation. The climatic changes over North Africa to the orbital forcing alone at 6 ka and 127 ka want to extend tropical xerophytic shrubland into the Sahara (see next paragraph). Incorporating shrub/savanna vegetation over the Sahara in Holocene simulations has been shown to impact the albedo and evapotranspiration of the surface and water budgets, reducing model and data mismatches (Pausata et al., 2016; Thompson et al., 2019). A vegetated Sahara would also reduce the dust loading over the Sahara. Previous modeling studies have come to different conclusions on the effects of this dust reduction on middle Holocene Saharan rainfall, depending on differences in the optical properties of dust, on whether changes in both dust and vegetation were considered, and whether indirect dust effects were also simulated. With only direct aerosol effects, Pausata et al. (2016) found an increase in Saharan rainfall with an assumed decreased dust loading at 6 ka, while Thompson et al. (2019) found that including the indirect effects of dust dampened this increase. With only direct aerosol effects (less absorbing dust in line with recent observational constraints) but no changes in vegetation, Albani and Mahowald (2019) found a positive feedback of dust on monsoon precipitation, fading as dust level are reduced during the midHolocene; on the other hand, using more absorbing dust would yield the opposite

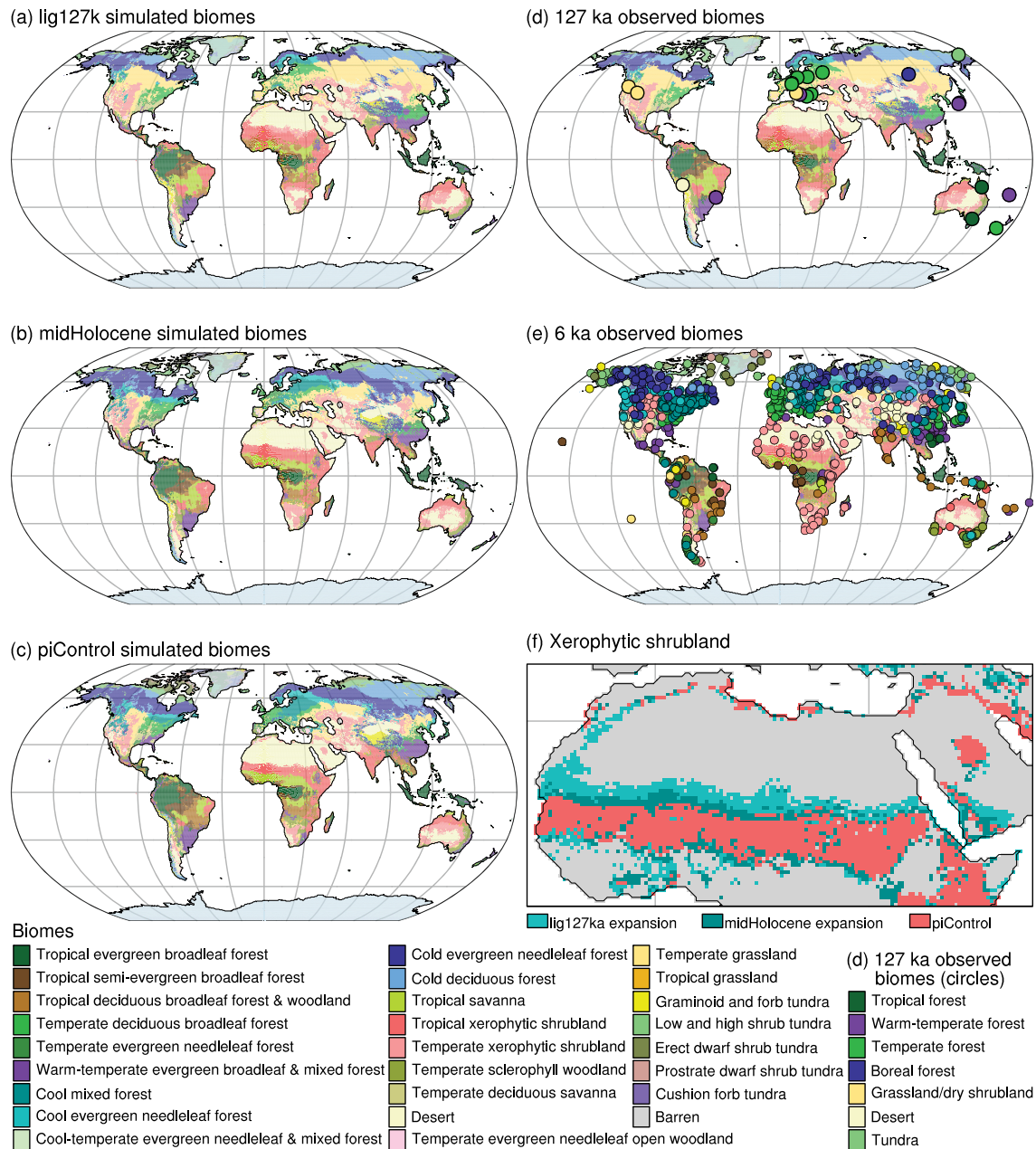


**Figure 14.** Global biomes simulated by BIOME4 and observed. Biomes simulated using temperature and precipitation data from CESM2 a) *lig127k*, b) *midHolocene*, and c) *piControl* experiments (Shafer et al., 2020). Observed biomes (circles) for d) 127 ka (Hoogakker et al., 2016; Tarasov et al., 2013) and e) 6 ka (Harrison, 2017) plotted on top of *lig127k* a) and *midHolocene* b) simulated biomes. f) Extent of temperate and tropical xerophytic shrubland for *piControl*, and its expansion for *midHolocene* and *lig127k*.

results. A previous modeling study suggests that soil feedback might also be important for driving the African monsoon northward during interglacials (Levis et al., 2004). As concluded by Hopcroft and Valdes (2019), there is no smoking gun in resolving this long-standing model-data mismatch.

### 5.3. Vegetation

Global terrestrial biomes simulated by BIOME4 (version 4.2; Kaplan et al., 2003) using CESM2 *midHolocene* and *lig127k* climate data generally match observed global vegetation patterns for 6 ka (Binney et al., 2017; BIOME 6000; Harrison, 2017) and 127 ka (Hoogakker et al., 2016; Tarasov et al., 2013; Figure 14), although observed vegetation proxy data for 127 ka are limited. The *midHolocene* and *lig127k* increases in JJA

temperatures for NH continents (Figure 3) result in expansion of temperate grassland and temperate xerophytic shrubland in North America and Eurasia, with the larger JJA temperature increases for *lig127k* (Figure 3) leading to expansion of grassland and shrubland over a larger area of North America and Eurasia than for *midHolocene* (Figure 14a and 14b). Warmer than present JJA temperatures also result in expansion of cold evergreen needleleaf forest northward in northern North America and northern Eurasia for *midHolocene* and *lig127k*. In eastern China, the northern limit of warm temperate evergreen broadleaf and mixed forest contracts south to  $\sim 30^\circ$  N for *midHolocene* and  $\sim 28^\circ$  N for *lig127k*. The northern limit of the CESM2 *midHolocene* warm temperate evergreen broadleaf and mixed forest is similar to that in CCSM4 6 ka biome simulations (Lin et al., 2019), but not as far north as observed for 6 ka (Ni et al., 2010). Although changes in atmospheric CO<sub>2</sub> concentrations may also affect biome distributions (e.g., Harrison & Prentice, 2003), the CO<sub>2</sub> concentrations used in the biome simulations for the *piControl*, *midHolocene*, and *lig127k* are similar (Table 1).

The CESM2-enhanced NH monsoons (Figure 4) produce biome shifts for *midHolocene* and *lig127k* compared to *piControl* (Figure 14). In North Africa, the northward shift of summer monsoon precipitation (Figure S5) leads to an increase in the northward extent of simulated temperate and tropical xerophytic shrubland vegetation in North Africa for both the *midHolocene* and *lig127k* compared to *piControl* (Figure 14f). The *midHolocene* shrubland expansion reaches  $\sim 20^\circ$  N, a similar extent as in CCSM3 mid-Holocene vegetation simulations (Herold et al., 2012). The *lig127k* shrubland expansion reaches  $\sim 22^\circ$  N across North Africa, with a strip of shrubland extending along the northwest edge of Africa to the Atlas Mountains. This northward expansion of vegetation in the Sahara for *midHolocene* and *lig127k* is consistent with interglacial vegetation reconstructions for the region (Jolly et al., 1998; Larrasoana et al., 2013), although the simulated biomes do not extend as far north across the Sahara as indicated by the reconstructions (Figures 14e and S5).

In the SH, CESM2 austral summer (DJF), temperatures are generally cooler than the *piControl* simulation for both the *midHolocene* and *lig127k* (Figure 3). In South America, tropical savanna and temperate and tropical xerophytic shrubland for *midHolocene* and *lig127k* expand compared to *piControl* (Figure 14). The *midHolocene* shift to more xeric vegetation is in general agreement with observations (Figure 14e; Marchant et al., 2009). In southern Africa, temperate xerophytic shrubland expands northward and eastward for *midHolocene* with expansion of desert for *lig127k*. Warm temperate evergreen broadleaf and mixed forest decreases in southeast Africa for *midHolocene* and *lig127k*, with the *midHolocene* decreases in general agreement with 6 ka observations (Figure 14b and 14e; Jolly et al., 1998).

#### 5.4. Sea Ice

The three model versions (CCSM3, CCSM4, CESM2) differ significantly in their simulations of *piControl*, *midHolocene*, and *lig127k* Arctic sea ice thicknesses and concentrations of Arctic summer (August–September) minima (Figure 15). In comparison to the earlier versions, CESM2 shows a greater response to the orbital-driven forcing of the MH and LIG simulations in Arctic summer minimum (August–September, AS) sea ice extent and concentrations. The CCSM3 MH and PMIP3 CCSM4 MH simulations show a much smaller change in Arctic summer minimum extent and area as compared to their preindustrial controls, whereas there is a noticeable reduction in summer minimum extent and area in the CESM2 *midHolocene*. The CESM2 *lig127k* shows a greater reduction in summer minimum extent and area as compared to the CCSM4 127 ka simulation.

The Arctic summer sea ice thickness shows more sensitivity to MH forcing than sea ice extent in CCSM4, but the reduction in thickness over the central Arctic appears to be less in CCSM4 ( $-28\%$ ) than occurs in CESM2 ( $-36\%$ ). The central Arctic minimum sea ice thickness in CCSM3 shows a similar large sensitivity to the PMIP2 MH forcing compared to the preindustrial control ( $-34\%$ ) as shown in the CESM2 *midHolocene*. The CCSM3 preindustrial control shows the thickest Arctic minimum summer sea ice. This may be because in CCSM3, a ‘present day’ simulation with present day (1990 CE) greenhouse gases and orbital parameters was used to tune the top of atmosphere imbalance. The CCSM3 preindustrial control was set up with 1780 CE greenhouse gases and modern orbital parameters which yielded a much thicker central Arctic sea ice in comparison as a result.

Paleo-sea ice distributions from marine cores collected in the Arctic Ocean, Nordic Seas, and northern North Atlantic are available for the Holocene and Last Interglacial based on dinocysts, foraminifers, ostracods, and

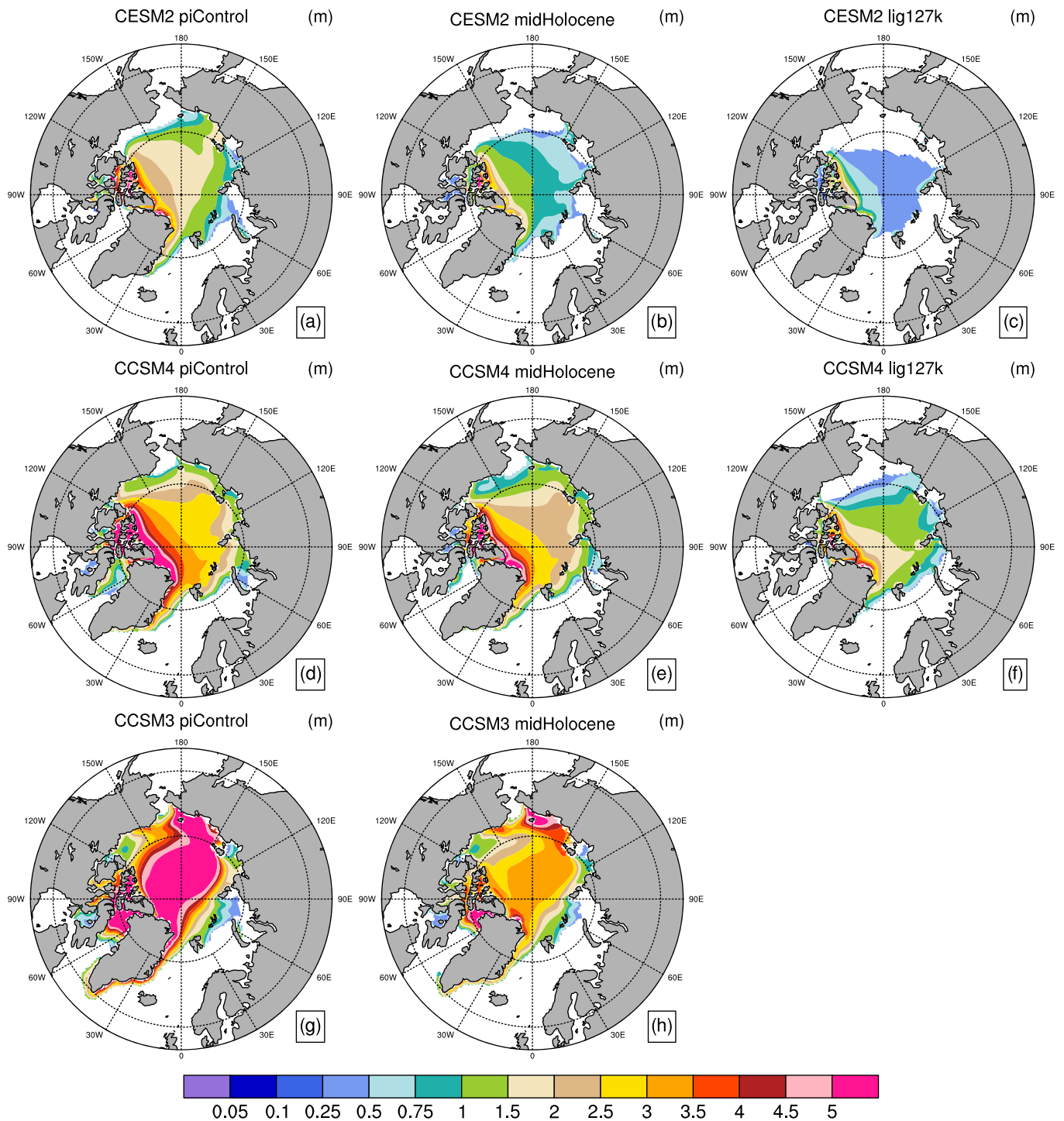


**Figure 15.** Northern Hemisphere Sea ice thickness (m) during August–September through multiple versions of CESM. Shown are the PI controls and 6 ka simulations for CCSM3, CCSM4, and CESM2 and the 127 ka simulations for CCSM4 and CESM2. Monthly data have been converted to the celestial calendar. Sea ice thickness is shown where sea ice grid box fractional area is greater than 15%.

biomarkers (Stein, Fahl, Gierz, et al., 2017; Stein, Fahl, Schade, et al., 2017; Kageyama et al., 2020), though with some differences in the interpretations based on the different indicators. Following the phytoplankton-IP<sub>25</sub> (PIP<sub>25</sub>) index of Müller et al. (2011), which combines the environmental information carried by IP<sub>25</sub> and other phytoplankton biomarkers, Stein, Fahl, Schade, et al. (2017) interpret the PIP<sub>25</sub> index as indicating

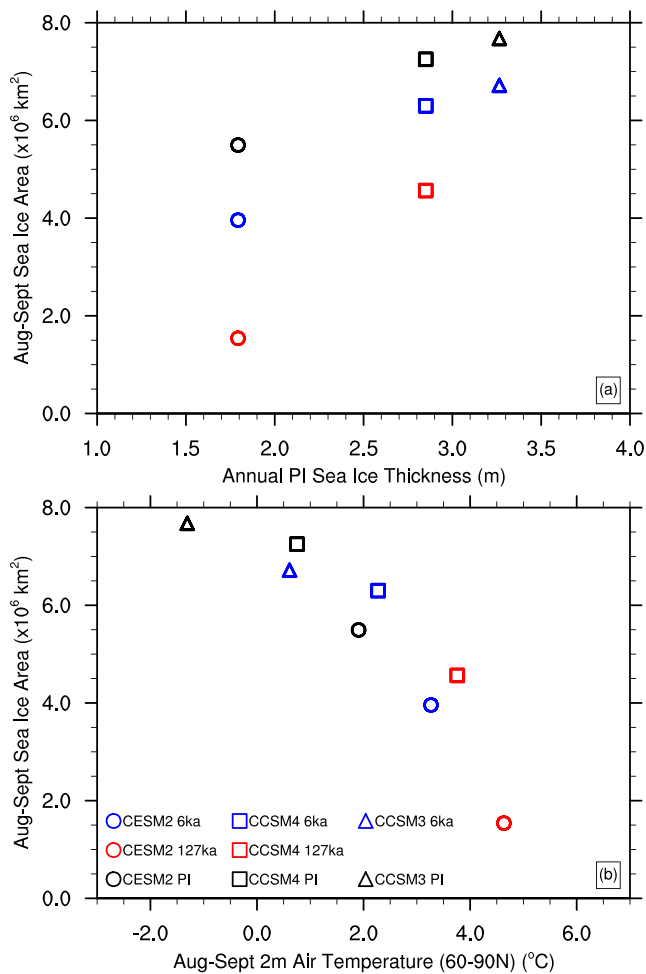


**Figure 16.** Scatter plots of minimum (August–September) Arctic Sea ice metrics through multiple versions of CESM. Sea ice area for concentrations >15% ( $10^6 \text{ km}^2$ ) versus a) *piControl* sea ice thickness (m) and b) August–September Arctic surface air temperatures ( $^{\circ}\text{C}$ ).

reduced sea ice cover (0.3 to 0.5), seasonal sea ice cover including ice-edge situation (0.5 to 0.7) and extended to perennial sea ice cover (>0.7). The synthesis documented in Kageyama et al. (2020) classifies sites in terms of number of minimum and maximum months with sea ice cover greater than 15%.

Stein, Fahl, Gierz, et al. (2017) conclude from their analysis of four ocean sediment cores in the Arctic (see Figure S6 and Supp. Table S2 for locations) dated to the LIG that for the three central Arctic sites perennial sea ice cover was probably predominant. Sea ice conditions were much more variable along the northern Barents Sea north of Svalbard and with the minimum sea ice concentrations towards almost ice-free summers. This agrees with the synthesis presented in Kageyama et al. (2020) that the three sites in the central Arctic were sea ice covered for at least 9 months and possibly perennial sea ice covered, and that the site north of Svalbard could have been ice free up to 6 months. The CESM2 *lig127k* simulation reproduces well the extent as interpreted in Kageyama et al. (2020), with one sea ice-free month (September) at the more southern sites (PS2138–2 and PS2757–8) but perennially sea ice covered at the two sites poleward of 85 N (Figure S7). The CCSM4 simulation retains sea ice perennially at all four sites. Interestingly, the CESM2 *midHolocene* has the southern sites at the sea-ice edge.

For four sites around the periphery of the Arctic Ocean (see Figure S6 and Supp. Table S2 for locations), the biomarker proxy records analyzed by Stein, Fahl, Schade, et al. (2017) show minimum sea ice extent during the early Holocene and reduced, seasonally sea ice at 6 ka. CESM2 *midHolocene* simulates extended sea ice-free (<15% concentration) conditions during the summer at the locations of the Chukchi and Fram Strait cores and much reduced September sea ice at the locations of the Siberian and Laptev cores (Figure S8). The CCSM4 and CCSM3 6 ka simulations retain sea ice perennially at all four sites.

Previous studies suggest that the mean-ice state in the control climate can influence the magnitude and spatial distribution of warming at high latitudes in future projections (Holland & Bitz, 2003). Thinner Arctic sea ice is more susceptible to summer melting than thicker Arctic sea ice. Across the family of CESM models, this relationship is clear with a correlation of

0.86 (Figure 16a). Arctic sea ice thickness, averaged for model grid cells with at least 15% concentration, varies substantially in the PI simulations, ranging from 3.2 m in CCSM3, 2.8 m in CCSM4, and 1.8 m in CESM2. CESM2 has much greater reductions in August–September minimum Arctic sea ice area at 6 ka and 127 ka than either CCSM4 or CCSM3.

There is a clear linear relationship between less Arctic sea ice coverage in August–September and warmer August–September average high northern latitude air temperature across the CESM family of models and for these three climate states (Figure 16b). This relationship, with a linear correlation coefficient of  $-0.91$ , is consistent with both the largest controlling processes, the albedo effect of sea ice on air temperatures and the insulating effect of sea ice on air-sea exchange. Reduced sea ice coverage lowers the average albedo of the Arctic surface, warming air temperatures and allowing increased ocean heat uptake, while also reducing the insulating effect of sea ice which allows increased air-sea heat exchange.

### 5.5. Dust Aerosols

As noted in Section 4.1.3, the *midHolocene* captures fairly well the observational constraints, represented by dust mass accumulation rates from paleodust archives integrated for the 6 ka time slice (5–7 ka) (Albani et al., 2015).

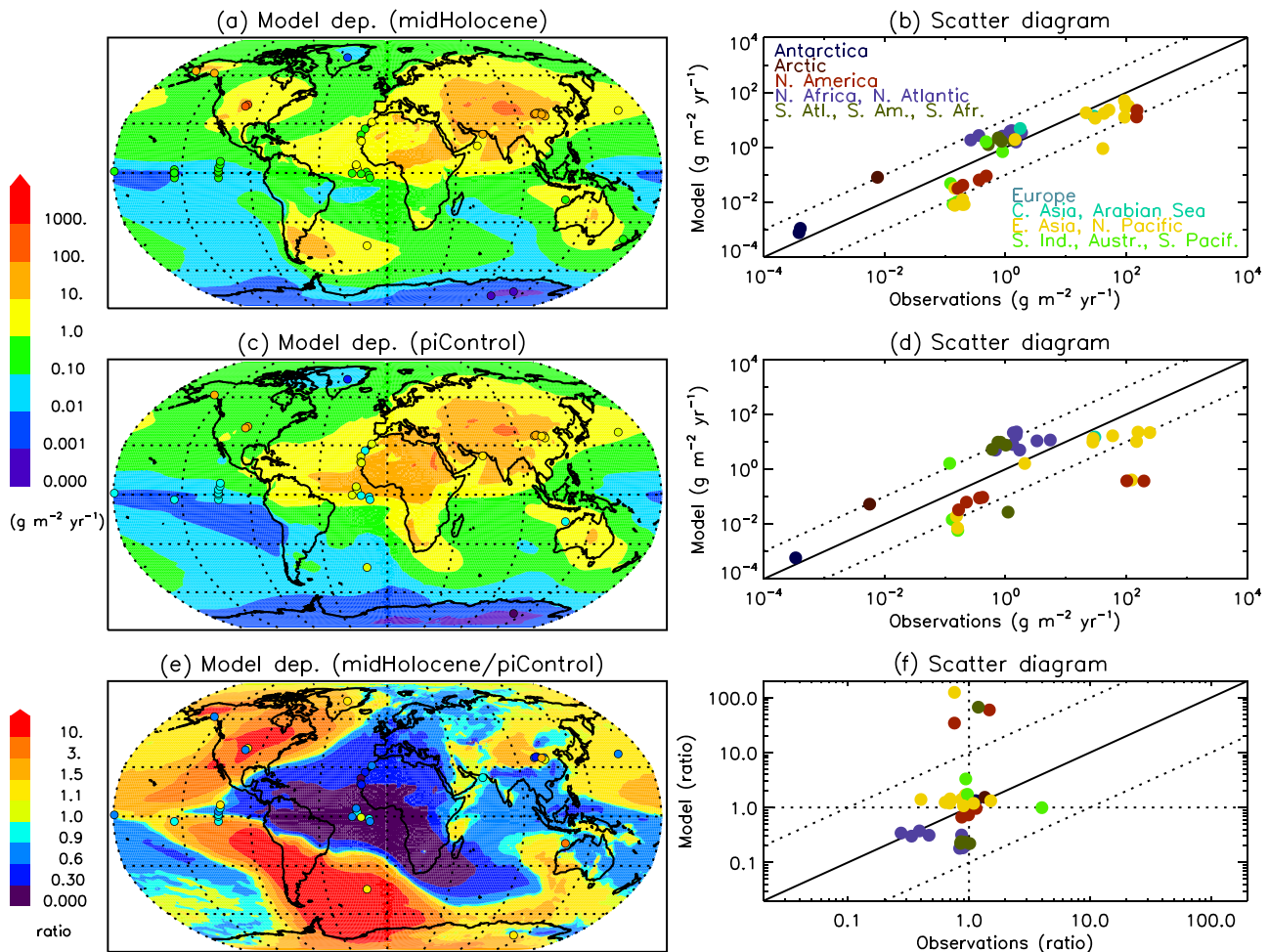


**Figure 17.** Comparison of simulated total (wet + dry) dust deposition against observational constraints from paleodust archives. (a,b) *midHolocene*, (c,d) *piControl*, and (e,f) the ratio *midHolocene/piControl*. On the left panels, contour maps represent model output, and filled circles represent observations, plotted using the same color scale. Panels on right depict scatterplots for the corresponding variables and time period, highlighting with colors the geographical locations of the paleodust archives used for the comparison. Dust mass accumulation rates used as observational constraints were integrated from the original time series between 5 and 7 ka for the *midHolocene*, and between 1 and 3 ka for the *piControl* case (Albani et al., 2015). The same analysis repeated using a subset of those observational records, with samples reaching into the last millennium, depict a similar picture (not shown).

The evaluation of dust deposition for the *piControl* case is more complicated, because of the scarcity and uncertainties of records encompassing this time period, as e.g. marine core tops are lost during the drilling process, and there may not be the temporal resolution required (Albani et al., 2016; Carslaw et al., 2017; Hooper & Marx, 2018; Mahowald et al., 2010). However, we can use dust mass accumulation rate estimates for the late Holocene as a loose constraint (Figure 17). In this case too, the overall fit of model results with data is reasonable for the most part, but when we compare the *midHolocene/piControl* ratio we see some significant deviations. Some of the discrepancies are probably due to the poorer fit of the model with data in the *piControl* case compared to the *midHolocene* case; in this respect we stress how the *piControl* soil erodibility map was not updated consistently with the *midHolocene* map, therefore without the constraint to match this middle to late Holocene ratio from the observations. In addition, we note how observations from the same region sometimes show opposing values of the *midHolocene/piControl* ratio (Figure 17e), which could be interpreted as either due to finer temporal and spatial scale features that cannot be captured by the model or by uncertainties in the observational estimates. In any case, we stress how our simulations capture the most relevant changes in the dust cycle, represented by the reduction of dust emissions from the Sahara (Figures 17e, 17f).

Previous work with CESM1 indicates a net perturbation of the global atmospheric radiative budget due to dust DRE (effective Direct Radiative Perturbation: eDRP) at the top of the atmosphere (TOA) of  $-0.06 \text{ W m}^{-2}$  and  $-0.03 \text{ W m}^{-2}$  for the *piControl* and *midHolocene*, respectively (Albani & Mahowald, 2019). Considering that these global budgets result from partial compensation of both positive and negative net perturbations at the TOA, the overall DRE perturbation to the atmospheric radiative budget was better expressed by the absolute values of  $0.27 \text{ W m}^{-2}$  (*piControl*) and  $0.23 \text{ W m}^{-2}$  (*midHolocene*), i.e. the global average of the absolute values of eDRP (Albani & Mahowald, 2019). The same study found that dust tends to enhance the West African monsoon, potentially acting as a negative feedback mechanism during the middle to late Holocene transition, i.e. as more humid conditions tend to suppress dust emissions—therefore reducing dust amplification of the monsoon.

In CESM2 a different aerosol scheme is used, i.e. a modal scheme with dust distributed in two modes and accounting for aerosol indirect effects, whereas the work previously done with CESM1 relied on a bulk aerosol scheme with no inclusion of indirect effects. Since diagnosing the impact of aerosol-cloud indirect effect requires additional simulations (Wang et al., 2011), which were not done here, we do not know the impact of the changes in dust on the liquid clouds and the resulting impact on radiative forcing, but these are likely to be small due to the small change in cloud condensation nuclei numbers from coarse mode dust particles (Mahowald et al., 2011).

## 6. Summary and Discussion

The *midHolocene* and *lig127k* experiments with CESM2 in CMIP6 and PMIP4 provide an out-of-sample assessment of the future projection experiments with CESM2. In concert with paleo-data for these time periods, they allow evaluations of the responses and connections within CESM2 to different radiative forcings. Particular foci of the *midHolocene* and *lig127k* experiments are high-latitude amplification of temperatures and low-latitude monsoon precipitation. They are also important for understanding and explaining past environments recorded in the geologic record.

The primary forcing for the *midHolocene* and *lig127k* are the orbitally induced changes in the seasonal and latitudinal distribution of insolation. In particular, the orbital configurations resulted in positive NH summer insolation anomalies at 6 ka and 127 ka as compared to PI. The anomalies are considerably greater at 127 ka than at 6 ka, associated with greater eccentricity and boreal summer solstice at perihelion at 127 ka. Atmospheric greenhouse gas levels were similar to those of the preindustrial period, land ice likely only remained over Greenland and Antarctica, and the continental configurations were almost identical to modern.

In response to the positive NH summer insolation anomalies, both experiments simulate JJA warming at NH middle and high latitudes (particularly over North America, Eurasia, and Greenland), reduced Arctic summer sea ice, and enhanced NH summer monsoon precipitation. These responses are greater in the *lig127k* than *midHolocene* simulation. Notably, the Arctic goes almost ice free in September in the *lig127k* simulation with thin sea ice in the central Arctic, and Greenland has much more extensive ablation zones in its western and northern coastal zones suggesting potential retreat if not fixed in the simulation. The *lig127k* simulation simulates the strong summer warming reconstructed for the Baffin region. Both the areal extent and cumulative rainfall is greater for the North African monsoon in the *lig127k* than *midHolocene* simulation (Brierley et al., 2020; Otto-Bliesner et al., 2020).

The most consistent regional pictures in the annual temperature reconstructions for 6 ka and 127 ka are the positive temperature anomalies over Greenland for both time periods and at 127 ka for Antarctica. CESM2 simulates the patterns but not the magnitudes of the reconstructed anomalies. Several regional features are in general agreement between the proxy records and the *midHolocene* simulation. These include east–west patterns of positive/negative 6 ka surface air temperature anomalies as compared to PI in eastern/western U.S., eastern China/Tibet, and western/eastern North Atlantic. The *lig127k* simulation also displays similar patterns but little data are available to confirm.

Vegetation integrates the effects of temperature and precipitation. Although the CESM2 *midHolocene* and *lig127k* simulations do not include predictive vegetation, the global terrestrial biomes simulated by BIOME4 using CESM2 *midHolocene* and *lig127k* climate data can be used for comparison to observed

global vegetation patterns. Warmer than present JJA temperatures result in expansion of cold evergreen needleleaf forest northward in northern North America and northern Eurasia for *midHolocene* and *lig127k*, in generally good agreement with pollen and macrofossil evidence. Xerophytic shrubland expands in northern Africa in the *midHolocene*, and even more so in the *lig127k* in response to the simulated greater area extent of cumulative rainfall of the North African monsoon. Comparison of the *midHolocene* simulated to the 6 ka observed biomes indicates that CESM2 underestimates this expansion.

Globally the largest differences in the barotropic ocean transport compared to the preindustrial control are found in the Southern Ocean and the North Atlantic, with a weaker Antarctic Circumpolar Current and strengthened North Atlantic subtropical and subpolar gyres in both paleoclimate states, but to a greater degree in the *lig127k* as compared to the *midHolocene*. The AMOC and AABW are only weakly sensitive to changes in the combined forcing from the seasonal and latitudinal redistribution of insolation.

Improvements in ENSO characteristics (period, amplitude, seasonal cycle) in CCSM4 as compared to CCSM3 are retained in CESM2, though the Niño3.4 SST index in the *piControl* simulation is overestimated by ~30%. The Niño3.4 index has reduced power going from the *piControl* to *midHolocene* to *lig127k*, with a 20% reduction in the Niño3.4 standard deviation in the *lig127k* as compared to the *piControl* and a much flatter annual cycle in the *lig127k* simulation. The seasonal cycle of Pacific equatorial SST strengthens in *lig127k* and weakens in *midHolocene* compared to the *piControl*. The seasonal anomalies in the eastern Pacific relative to the seasonal cycle of the *piControl* appear phased with tropical insolation anomalies. Colder annual mean SST across the tropics plus enhanced seasonal cooling in DJF with respect to the *piControl*, especially notable in *lig127k*, may be responsible for muting ENSO events which tend to peak at the end of the year.

Model differences are considerable between the older versions of the models (CCSM3 and CCSM4) and CESM2, which are associated with significant improvements made in the physics of the component models and resolutions of the simulations. The summer monsoon over North Africa intensifies and shifts northward in the three model versions, though, less so than indicated by observed biomes. The family of models agree on warmer summers at middle and high NH latitudes with this warming greater at 127 ka than 6 ka. Differences in the polar surface temperature anomalies are related to simulation of sea ice thickness and extent in the respective preindustrial simulations with CESM2 having an improved reproduction of these features as compared to observationally-based estimates (Danabasoglu et al., 2020).

The selection of only two intervals, *midHolocene* and *lig127k*, for CMIP6-PMIP4 Tier1 simulations was designed to maximize both the multi-model ensemble size and opportunities for model evaluation with data syntheses. Indeed, 13 *midHolocene* and 17 *lig127k* simulations were contributed by modeling centers to CMIP6. Uncertainties in the boundary and initial conditions for the MH and LIG as well as missing processes in CESM2, and in simulations by many other modeling groups, may be important for explaining mismatches with the data. These will be explored in future experiments with CESM2.

Recognizing this, PMIP proposed CMIP6 Tier 2 sensitivity experiments for the *midHolocene* and *lig127k* to explore the feedbacks between vegetation and climate: *midHolocene-veg* and *lig127k-veg* (Otto-Bliesner et al., 2017). Reconstructions indicate that xerophytic shrubland (Figures 14 and S5) extended into the Sahara. Previous modeling studies suggest that incorporating shrub/savanna vegetation over the Sahara as well as soil feedbacks in CCSM/CESM are important for the northward extension of the African monsoon during the Holocene (Levis et al., 2004; Thompson et al., 2019). Replacement of tundra with boreal forests over the NH high-latitude continents, as indicated by pollen and macrofossil data (Figure 14), amplifies high-latitude warming in CCSM/CESM simulations (Feng et al., 2020; Swann et al., 2010). In addition, a new optional feature in the CESM land model is the demographically structured dynamic vegetation model (Functionally Assembled Terrestrial Ecosystem Simulator), which will allow prediction of biome boundaries directly from plant physiological traits (Fisher et al., 2019; Lawrence et al., 2019).

Matches of the CESM2 *lig127k* simulation and data reconstructions could be affected by both the design of the CMIP6 experiment and uncertainties in the dating of the LIG records. The 127 ka time slice for the CMIP6-PMIP4 LIG experiment was chosen to account for dating uncertainties and the imprint of the previous deglaciation and Heinrich 11 (H11) meltwater event on temperature. Data reconstructions for 127 ka (Figures 12 and 13) suggest that the bipolar response of the climate system to melting of the NH ice sheets, with cold surface temperature anomalies in the North Atlantic and warm surface temperature

anomalies over the Southern Ocean and Antarctica, may still be present at 127 ka. In addition, the *lig127k* simulation protocols included the Greenland and Antarctic ice sheets prescribed as modern. However, it is possible that the West Antarctic Ice Sheet retreated early in the LIG and that the Greenland ice sheet was reduced in extent as compared to present. The CMIP6 Tier 2 sensitivity experiments: *lig127k-H11*, *lig127k-ais*, and *lig127k-gris*, will allow the effects of these uncertain protocols to be explored. In addition, a transient LIG simulation is providing an opportunity to examine the time-dependent evolution of the climate and Greenland ice sheet in CESM and CISM to the LIG orbital forcing.

The CESM community has been participating in about 20 CMIP6-endorsed MIPs, with results documented in the *AGU CESM2 Virtual Special Issue* ([https://agupubs.onlinelibrary.wiley.com/doi/toc/10.1002/\(ISSN\)1942-2466.CESM2](https://agupubs.onlinelibrary.wiley.com/doi/toc/10.1002/(ISSN)1942-2466.CESM2)). The CESM2 *lig127k* and *midHolocene* experiments have potential implications for confidence in future projection simulations with CESM2 (DeRepentigny et al., 2020; Meehl et al., 2020). More than half of the 17 CMIP6 *lig127k* simulations have a retreat of the Arctic minimum (August–September) ice edge similar to the average of the last two decades (Otto-Bliesner et al., 2020). Across these CMIP6 models, Kageyama et al. (2020) noted a nearly linear relationship between the simulations of Arctic summer sea ice in their *1pctCO2* simulation at time of doubling and their *lig127k* simulations. That is, the models which respond strongly to the LIG forcing also respond strongly to the 1pctCO2 forcing. CESM2 has a high equilibrium climate sensitivity (ECS) of 5.3 °C (Gettelman et al., 2019); HadGEM3 similarly has a high ECS of 5.5 °C. Both predict an almost ice-free or ice-free Arctic in their *lig127k* experiments and the predicted year of disappearance of September sea ice in the SSP8–8.5 scenario of 2038 and 2035, respectively (Guarino et al., 2020). The CMIP6 and PMIP4 paleoclimate simulations with CESM2 combined with proxy reconstructions allow an assessment of whether this high ECS is plausible (Feng et al., 2020; Zhu et al., 2020).

With the availability of LIG ice and marine core records, the transient CESM2-CISM2 LIG simulation with an evolving Greenland ice sheet can inform the ISMIP6 future projection simulations with CESM2 and their predictions of sea level rise. The CMIP6 (and CESM2) paleoclimate simulations thus provide an opportunity to better constrain projections of future climate change.

## Data Availability Statement

CESM2 is freely available at <http://www.cesm.ucar.edu/models/cesm2/>. Simulation data for CESM2 used in this study are freely available from the Earth System Grid Federation (ESGF) at [esgf-node.llnl.gov/search/cmip6](https://esgf-node.llnl.gov/search/cmip6) and CCSM4 from the Climate Data Gateway at NCAR at <https://www.earthsystemgrid.org/>.

## Acknowledgments

We thank Alan Haywood and Chris Brierley, two anonymous reviewers, and the editor for their helpful comments and suggestions. The CESM project is supported primarily by the National Science Foundation (NSF). This material is based upon work supported by the National Center for Atmospheric Research, which is a major facility sponsored by the NSF under Cooperative Agreement No. 1852977. Computing and data storage resources, including the Cheyenne supercomputer (doi:10.5065/D6RX99HX), were provided by the Computational and Information Systems Laboratory (CISL) at NCAR. S. S. was supported by the U.S. Geological Survey Climate Research and Development Program. Any use of trade, firm, or product names is for descriptive purposes only and does not imply endorsement by the U.S. Government.

## References

- Albani, S., & Mahowald, N. M. (2019). Paleodust insights into dust impacts on climate. *Journal of Climate*, *32*(22), 7897–7913. <https://doi.org/10.1175/JCLI-D-18-0742.1>
- Albani, S., Mahowald, N. M., Murphy, L. N., Raiswell, R., Moore, J. K., Anderson, R. F., et al. (2016). Paleodust variability since the last glacial maximum and implications for iron inputs to the ocean. *Geophysical Research Letters*, *43*, 3944–3954. <https://doi.org/10.1002/2016GL067911>
- Albani, S., Mahowald, N. M., Perry, A. T., Scanza, R. A., Zender, C. S., Heavens, N. G., et al. (2014). Improved dust representation in the community atmosphere model. *Journal of Advances in Modeling Earth Systems*, *6*, 541–570. <https://doi.org/10.1002/2013MS000279>
- Albani, S., Mahowald, N. M., Winckler, G., Anderson, R. F., Bradtmiller, L. I., Delmonte, B., et al. (2015). Twelve thousand years of dust: The Holocene global dust cycle constrained by natural archives. *Climate of the Past*, *11*(6), 869–903. <https://doi.org/10.5194/cp-11-869-2015>
- Barlow, N. L. M., McClymont, E. L., Whitehouse, P. L., Stokes, C. R., Jamieson, S. S. R., Woodroffe, S. A., et al. (2018). Lack of evidence for a substantial sea-level fluctuation within the last interglacial. *Nature Geoscience*, *11*(9), 627–634. <https://doi.org/10.1038/s41561-018-0195-4>
- Bartlein, P. J., Harrison, S. P., Brewer, S., Connor, S., Davis, B. A. S., Gajewski, K., et al. (2011). Pollen-based continental climate reconstructions at 6 and 21 ka: A global synthesis. *Climate Dynamics*, *37*(3–4), 775–802. <https://doi.org/10.1007/s00382-010-0904-1>
- Bartlein, P. J., & Shafer, S. L. (2019). Paleo calendar-effect adjustments in time-slice and transient climate-model simulations (PaleoCalAdjust v1.0): Impact and strategies for data analysis. *Geoscientific Model Development*, *12*(9), 3889–3913. <https://www.geoscientific-model-dev.net/12/3889/2019/>, <https://doi.org/10.5194/gmd-12-3889-2019>
- Berger, A., & Loutre, M. F. (1991). Insolation values for the climate of the last 10 million years. *Quaternary Science Reviews*, *10*, 297–317. [https://doi.org/10.1016/0277-3791\(91\)90033-q](https://doi.org/10.1016/0277-3791(91)90033-q)
- Binney, H., Edwards, M., Macias-Fauria, M., Lozhkin, A., Anderson, P., Kaplan, J. O., et al. (2017). Vegetation of Eurasia from the last glacial maximum to present: Key biogeographic patterns. *Quaternary Science Reviews*, *157*, 80–97. <https://doi.org/10.1016/j.quascirev.2016.11.022>

- Bogenschutz, P. A., Gettelman, A., Morrison, H., Larson, V. E., Craig, C., & Schanen, D. P. (2013). Higher-order turbulence closure and its impact on climate simulation in the community atmosphere model. *Journal of Climate*, *26*(23), 9655–9676. <https://doi.org/10.1175/JCLI-D-13-00075.1>
- Braconnot, P., Harrison, S. P., Kageyama, M., Bartlein, P. J., Masson-Delmotte, V., Abe-Ouchi, A., et al. (2012). Evaluation of climate models using palaeoclimatic data. *Nature Climate Change*, *2*(6), 417–424. <https://doi.org/10.1038/nclimate1456>
- Braconnot, P., Otto-Bliesner, B., Harrison, S., Joussaume, S., Peterschmitt, J.-Y., Abe-Ouchi, A., et al. (2007). Results of PMIP2 coupled simulations of the mid-Holocene and last glacial maximum – Part 1: Experiments and large-scale features. *Climate of the Past*, *3*(2), 261–277. <https://doi.org/10.5194/cp-3-261-2007>
- Brady, E. C., Otto-Bliesner, B. L., Kay, J. E., & Rosenbloom, N. A. (2013). Sensitivity to glacial forcing in the CCSM4. *Journal of Climate*, *26*(6), 1901–1925. <https://doi.org/10.1175/JCLI-D-11-00416.1>
- Brierley, C. M., Zhao, A., Harrison, S. P., Braconnot, P., Williams, C. J. R., Thornalley, D. J. R., et al. (2020). Large-scale features and evaluation of the PMIP4-CMIP6 midHolocene simulations. *Climate of the Past Discussions*, *16*(5), 1847–1872. <https://doi.org/10.5194/cp-2019-168>
- Carslaw, K. S., Gordon, H., Hamilton, D. S., Johnson, J. S., Regayre, L. A., Yoshioka, M., & Pringle, K. J. (2017). Aerosols in the pre-industrial atmosphere. *Current Climate Change Report*, *3*(1), 1–15. <https://doi.org/10.1007/s40641-017-0061-2>
- Coe, M. T., & Harrison, S. P. (2002). The water balance of northern Africa during the mid-Holocene: An evaluation of the 6 ka BP PMIP simulations. *Climate Dynamics*, *19*(2), 155–166. <https://doi.org/10.1007/s00382-001-0219-3>
- COHMAP Members (1988). Climatic changes of the last 18,000 years: Observations and model simulations. *Science*, *241*(4869), 1043–1052. <https://doi.org/10.1126/science.241.4869.1043>
- Danabasoglu, G., Lamarque, J.-F., Bacmeister, J., Bailey, D. A., DuVivier, A. K., Edwards, J., et al. (2020). The community earth system model version 2 (CESM2). *Journal of Advances in Modeling Earth Systems*, *12*, e2019MS001916. <https://doi.org/10.1029/2019MS001916>
- DeRepentigny, P., Jahn, A., Holland, M. M., & Smith, A. (2020). Arctic Sea ice in two configurations of the community earth system model version 2 (CESM2) during the 20<sup>th</sup> and 21<sup>st</sup> centuries. *Journal of Geophysical Research: Oceans*, *125*, e2020JC016133. <https://doi.org/10.1029/2020JC016133>
- Emile-Geay, J., Cobb, K. M., Carré, M., Braconnot, P., Leloup, J., Zhou, Y., et al. (2016). Links between tropical Pacific seasonal, interannual and orbital variability during the Holocene. *Nature Geoscience*, *9*(2), 168–173. <https://doi.org/10.1038/ngeo2608>
- Eyring, V., Bony, S., Meehl, G. A., Senior, C. A., Stevens, B., Stouffer, R. J., & Taylor, K. E. (2016). Overview of the Coupled Model Intercomparison Project phase 6 (CMIP6) experimental design and organization. *Geoscientific Model Development*, *9*(5), 1937–1958. <https://doi.org/10.5194/gmd-9-1937-2016>
- Feng, R., Otto-Bliesner, B. L., Brady, E. C., & Rosenbloom, N. (2020). Increased climate response and earth system sensitivity from CCSM4 to CESM2 in mid-Pliocene simulations. *Journal of Advances in Modeling Earth Systems*, *12*, e2019MS002033. <https://doi.org/10.1029/2019MS002033>
- Fisher, R. A., Wieder, W. R., Sanderson, B., Koven, C. D., Oleson, K. W., Xu, C., et al. (2019). Parametric controls on vegetation responses to biogeochemical forcing in the CLM5. *Journal of Advances in Modeling Earth Systems*, *11*, 2879–2895. <https://doi.org/10.1029/2019MS001609>
- Folland, C. K., Karl, T. R., & Vinnikov, K. Y. (1990). Observed climate variations and change. In J. T. Houghton, G. J. Jenkins, J. Ephraums (Eds.), *Climate Change: The IPCC Scientific Assessment* (pp. 195–238). New York: Cambridge Univ. Press.
- Gettelman, A., Hannay, C., Bacmeister, J. T., Neale, R. B., Pendergrass, A. G., Danabasoglu, G., et al. (2019). High climate sensitivity in the community earth system model version 2 (CESM2). *Geophysical Research Letters*, *46*, 8329–8337. <https://doi.org/10.1029/2019GL083978>
- Gettelman, A., & Morrison, H. (2015). Advanced two-moment bulk microphysics for global models. Part I: Off-line tests and comparison with other schemes. *Journal of Climate*, *28*(3), 1268–1287. <https://doi.org/10.1175/JCLI-D-14-00102.1>
- Guarino, M.-V., Sime, L. C., Schröder, D., Malmierca-Vallet, I., Rosenblum, E., Ringer, M., et al. (2020). Sea-ice-free Arctic during the last interglacial supports fast future loss. *Nature Climate Change*, *10*(10), 928–932. <https://doi.org/10.1038/s41558-020-0865-2>
- Harrison, S. P. (2017). BIOME 6000 DB Classified Plotfile Version 1. Univ. of Reading. Dataset. <https://doi.org/10.17864/1947.99>
- Harrison, S. P., Jolly, D., Laarif, F., Abe-Ouchi, A., Dong, B., Herterich, K., et al. (1998). Intercomparison of simulated global vegetation distributions in response to 6 kyr BP orbital forcing. *Journal of Climate*, *11*(11), 2721–2742. [https://doi.org/10.1175/1520-0442\(1998\)011%3c2721:IOSGVD%3e2.0.CO;2](https://doi.org/10.1175/1520-0442(1998)011%3c2721:IOSGVD%3e2.0.CO;2)
- Harrison, S. P., & Prentice, I. C. (2003). Climate and CO<sub>2</sub> controls on global vegetation distribution at the last glacial maximum: Analysis based on palaeovegetation data, biome modelling and palaeoclimate simulations. *Global Change Biology*, *9*(7), 983–1004. <https://doi.org/10.1046/j.1365-2486.2003.00640.x>
- Herold, N., Yin, Q. Z., Karami, M. P., & Berger, A. (2012). Modelling the climatic diversity of the warm interglacials. *Quaternary Science Reviews*, *56*, 126–141. <https://doi.org/10.1016/j.quascirev.2012.08.020>
- Holland, M. M., & Bitz, C. M. (2003). Polar amplification of climate change in coupled models. *Climate Dynamics*, *21*(3–4), 221–232. <https://doi.org/10.1007/s00382-003-0332-6>
- Hoogakker, B. A. A., Smith, R. S., Singarayer, J. S., Marchant, R., Prentice, I. C., Allen, J. R. M., et al. (2016). Terrestrial biosphere changes over the last 120 kyr. *Climate of the Past*, *12*(1), 51–73. <https://doi.org/10.5194/cp-12-51-2016>
- Hooper, J., & Marx, S. (2018). A global doubling of dust emissions during the Anthropocene? *Global and Planetary Change*, *169*, 70–91. <https://doi.org/10.1016/j.gloplacha.2018.07.003>
- Hopcroft, P. O., & Valdes, P. J. (2019). On the role of dust-climate feedbacks during the mid-Holocene. *Geophysical Research Letters*, *46*, 1612–1621. <https://doi.org/10.1029/2018GL080483>
- Hunke, E. C., Lipscomb, W. H., Turner, A. K., Jeffery, N., & Elliott, S. (2015). CICE: The Los Alamos Sea Ice Model. Documentation and Software User's Manual. Version 5.1. T-3 Fluid Dynamics Group, Los Alamos National Laboratory, Tech. Rep. LA-CC-06-012.
- Jansen, E., Overpeck, J., Briffa, K. R., Duplessy, J. C., Joos, F., Masson-Delmotte, V., et al. (2007). Chapter 6: Palaeoclimate. In S. Solomon et al. (Eds.), *Climate Change 2007: The Physical Science Basis. Contribution of Working Group I to the Fourth Assessment Report of the Intergovernmental Panel on Climate Change* (pp. 433–498). Cambridge, United Kingdom and New York, NY, USA: Cambridge University Press.
- Jolly, D., Prentice, I. C., Bonnefille, R., Ballouche, A., Bengo, M., Brenac, P., et al. (1998). Biome reconstruction from pollen and plant macrofossil data for Africa and the Arabian peninsula at 0 and 6000 years. *Journal of Biogeography*, *25*(6), 1007–1027. <https://doi.org/10.1046/j.1365-2699.1998.00238.x>
- Joussaume, S., Taylor, K. E., Braconnot, P., Mitchell, J. F. B., Kutzbach, J. E., Harrison, S. P., et al. (1999). Monsoon changes for 6000 years ago: Results of 18 simulations from the Paleoclimate Modeling Intercomparison Project (PMIP). *Geophysical Research Letters*, *26*(7), 859–862. <https://doi.org/10.1029/1999GL00126>

- Kageyama, M., Braconnot, P., Harrison, S. P., Haywood, A. M., Jungclauss, J. H., Otto-Bliesner, B. L., et al. (2018). The PMIP4 contribution to CMIP6 – Part 1: Overview and over-arching analysis plan. *Geoscientific Model Development*, *11*(3), 1033–1057. <https://doi.org/10.5194/gmd-11-1033-2018>
- Kageyama, M. L., Sime, C., Sicard, M., Guarino, M.-V., de Vernal, A., Schroeder, D., et al. (2020). A multi-model CMIP6 study of Arctic Sea ice at 127 ka: Sea ice data compilation and model differences. *Climate of the Past Discussions*. <https://doi.org/10.5194/cp-2019-165>
- Kaplan, J. O., Bigelow, N. H., Prentice, I. C., Harrison, S. P., Bartlein, P. J., Christensen, T. R., et al. (2003). Climate change and Arctic ecosystems: 2. Modeling, paleodata-model comparisons, and future projections. *Journal of Geophysical Research*, *108*(D19), 8171. <https://doi.org/10.1029/2002JD002559>
- Kaufman, D., McKay, N., Routsom, C., Erb, M., Davis, B., Heiri, O., et al. (2020). A global database of Holocene paleotemperature records. *Scientific Data*, *7*(1), 115. <https://doi.org/10.1038/s41597-020-0445-3>
- Landrum, L., Otto-Bliesner, B. L., Wahl, E. R., Conley, A., Lawrence, P., Rosenbloom, N., & Teng, H. (2013). Last millennium climate and its variability in CCSM4. *Journal of Climate*, *26*(4), 1085–1111. <https://doi.org/10.1175/JCLI-D-11-00326.1>
- Larrasoana, J. C., Roberts, A. P., & Rohling, E. J. (2013). Dynamics of green Sahara periods and their role in hominin evolution. *PLoS ONE*, *8*, e76514. <https://doi.org/10.1371/journal.pone.0076514>
- Lawrence, D. M., Fisher, R. A., Koven, C. D., Oleson, K. W., Swenson, S. C., Bonan, G., et al. (2019). The Community Land Model Version 5: Description of new features, benchmarking, and impact of forcing uncertainty. *Journal of Advances in Modeling Earth Systems*, *11*, 4245–4287. <https://doi.org/10.1029/2018MS001583>
- Lawrence, D. M., Hurtt, G. C., Arneth, A., Brovkin, V., Calvin, K. V., & Jones, A. D. (2016). The land use model Intercomparison project (LUMIP) contribution to CMIP6: Rationale and experimental design. *Geoscientific Model Development*, *9*(9), 2973–2998. <https://doi.org/10.5194/gmd-9-2973-2016>
- Levis, S., Bonan, G. B., & Bonfils, C. (2004). Soil feedback drives the mid-Holocene north African monsoon northward in fully coupled simulations with a dynamic vegetation model. *Climate Dynamics*, *23*(7–8), 791–802. <https://doi.org/10.1007/s00382-004-0477-y>
- Lin, Y., Ramstein, G., Wu, H., Rani, R., Braconnot, P., Kageyama, M., et al. (2019). Mid-Holocene climate change over China: Model-data discrepancy. *Climate of the Past*, *15*(4), 1223–1249. <https://doi.org/10.5194/cp-15-1223-2019>
- Lipscomb, W. H., Fyke, J. G., Vizcaino, M., Sacks, W. J., Wolfe, J., Versteinsten, M., et al. (2013). Implementation and initial evaluation of the glimmer community ice sheet model in the community earth system model. *Journal of Climate*, *26*(19), 7352–7371. <https://doi.org/10.1175/JCLI-D-12-00557.1L>
- Liu, X., Ma, P.-L., Wang, H., Tilmes, S., Singh, B., Easter, R. C., et al. (2016). Description and evaluation of a new four-mode version of the modal aerosol module (MAM4) within version 5.3 of the community atmosphere model. *Geoscientific Model Development*, *9*(2), 505–522. <https://doi.org/10.5194/gmd-9-505-2016>
- Lunt, D. J., Abe-Ouchi, A., Bakker, P., Berger, A., Braconnot, P., Charbit, S., et al. (2013). A multi-model assessment of last interglacial temperatures. *Climate of the Past*, *9*(2), 699–717. <https://doi.org/10.5194/cp-9-699-2013>
- Mahowald, N., Ward, D. S., Kloster, S., Flanner, M. G., Heald, C. L., Heavens, N. G., et al. (2011). Aerosol impacts on climate and biogeochemistry. *Annual Review of Environment and Resources*, *36*(1), 45–74. <https://doi.org/10.1146/annurev-enviro-042009-094507>
- Mahowald, N. M., Kloster, S., Engelstaedter, S., Moore, J. K., Mukhopadhyay, S., McConnell, J. R., et al. (2010). Observed 20th century desert dust variability: Impact on climate and biogeochemistry. *Atmospheric Chemistry and Physics*, *10*(22), 10,875–10,893. <https://doi.org/10.5194/acp-10-10875-2010>
- Mahowald, N. M., Muhs, D. R., Levis, S., Rasch, P. J., Yoshioka, M., Zender, C. S., & Luo, C. (2006). Change in atmospheric mineral aerosols in response to climate: Last glacial period, preindustrial, modern, and doubled carbon dioxide climates. *Journal of Geophysical Research*, *111*, D10202. <https://doi.org/10.1029/2005JD006653>
- Marchant, R. A., Cleef, A., Harrison, S. P., Hooghiemstra, H., Markgraf, V., van Boxel, J., et al. (2009). Pollen-based biome reconstructions for Latin America at 0, 6000 and 18 000 radiocarbon years ago. *Climate of the Past*, *5*(4), 725–767. <https://doi.org/10.5194/cp-5-725-2009>
- Marino, G., Rohling, E. J., Rodriguez-Sanz, L., Grant, K. M., Heslop, D., Roberts, A. P., et al. (2015). Bipolar seesaw control on last interglacial sea level. *Nature*, *522*(7555), 197–201. <https://doi.org/10.1038/nature14499>
- Masson-Delmotte, V., Schulz, M., Abe-Ouchi, A., Beer, J., Ganopolski, A., Gonzalez Rouco, J., et al. (2013). Chapter 5: Information from paleoclimate archives. In T. F. Stocker et al. (Eds.), *Climate Change 2013: The Physical Science Basis. Contribution of Working Group I to the Fifth Assessment Report of the Intergovernmental Panel on Climate Change* (pp. 383–464). Cambridge, United Kingdom and New York, NY, USA: Cambridge University Press.
- McAvaney, B. J., Covey, C., Joussaume, S., Kattsov, V., Kitoh, A., Ogana, W., et al. (2001). Chapter 8: Model Evaluation. In J. T. Houghton, et al. (Eds.), *Climate Change 2001: The Scientific Basis. Contribution of Working Group I to the Third Assessment Report of the Intergovernmental Panel on Climate Change* (pp. 471–524). Cambridge, United Kingdom and New York, NY, USA: Cambridge University Press.
- Meehl, G. A., Arblaster, J. M., Bates, S., Richter, J. H., Tebaldi, C., Gettelman, A., et al. (2020). Characteristics of future warmer base states in CESM2. *Journal of Advances in Modeling Earth Systems*, *7*, e2020EA001296. <https://doi.org/10.1029/2020EA001296>
- Müller, J., Wagner, A., Fahl, K., Stein, R., Prange, M., & Lohmann, G. (2011). Towards quantitative sea ice reconstructions in the northern North Atlantic: A combined biomarker and numerical modelling approach. *Earth and Planetary Science Letters*, *306*(3–4), 137–148. <https://doi.org/10.1016/j.epsl.2011.04.011>
- Ni, J., Yu, G., Harrison, S. P., & Prentice, I. C. (2010). Palaeovegetation in China during the late Quaternary: Biome reconstructions based on a global scheme of plant functional types. *Palaeogeography, Palaeoclimatology, Palaeoecology*, *289*(1–4), 44–61. <https://doi.org/10.1016/j.palaeo.2010.02.008>
- Otto-Bliesner, B. L. (1999). El Niño/La Niña and Sahel precipitation during the middle Holocene. *Geophysical Research Letters*, *26*(1), 87–90. <https://doi.org/10.1029/1998GL900236>
- Otto-Bliesner, B. L., Braconnot, P., Harrison, S. P., Lunt, D. J., Abe-Ouchi, A., Albani, S., et al. (2017). The PMIP4 contribution to CMIP6 – Part 2: Two interglacials, scientific objective and experimental design for Holocene and last interglacial simulations. *Geoscientific Model Development*, *10*(11), 3979–4003. <https://doi.org/10.5194/gmd-10-3979-2017>
- Otto-Bliesner, B. L., Brady, E. C., Clauzet, G., Tomas, R., Levis, S., & Kothavala, Z. (2006). Last glacial maximum and Holocene climate in CCSM3. *Journal of Climate*, *19*(11), 2526–2544. <https://doi.org/10.1175/JCLI3748.1>
- Otto-Bliesner, B. L., Brady, E. C., Zhao, A., Brierley, C., Axford, Y., Capron, E., et al. (2020). Large-scale features of last interglacial climate: Results from evaluating the *lig127k* simulations for CMIP6-PMIP4. *Climate of the Past Discussions*. <https://doi.org/10.5194/cp-2019-174>
- Pausata, F. S. R., Messori, G., & Zhang, Q. (2016). Impacts of dust reduction on the northward expansion of the African monsoon during the green Sahara period. *Earth Planet Science Letters*, *434*, 298–307. <https://doi.org/10.1016/j.epsl.2015.11.049>

- Power, M. J., Marlon, J., Ortiz, N., Bartlein, P. J., Harrison, S. P., Mayle, F., et al. (2008). Changes in fire regimes since the last glacial maximum: An assessment based on a global synthesis and analysis of charcoal data. *Climate Dynamics*, *6*(2), 549–561. <https://doi.org/10.1007/s00382-007-0334-x>
- Rosenbloom, N. A., Otto-Bliesner, B. L., Brady, E. C., & Lawrence, P. J. (2013). Simulating the mid-Pliocene warm period with the CCSM4 model. *Geoscientific Model Development*, *6*(2), 549–561. <https://doi.org/10.5194/gmd-6-549-2013>
- Scussolini, P., Bakker, P., Guo, C., Stepanek, C., Zhang, Q., Braconnot, P., et al. (2019). Agreement between reconstructed and modeled boreal precipitation of the last interglacial. *Science Advances*, *5*, eaax7047. <https://doi.org/10.1126/sciadv.aax7047>
- Serreze, M. C., & Barry, R. G. (2011). Processes and impacts of Arctic amplification: A research synthesis. *Global and Planetary Change*, *77*(1–2), 85–96. <https://doi.org/10.1016/j.gloplacha.2011.03.004>
- Shafer, S. L., Bartlein, P. J., Otto-Bliesner, B. L., & Brady, E. C. (2020). Biomes simulated by BIOME4 using CESM2 *lig127k*, *midHolocene*, and *piControl* climate data on a global 0.5-degree grid, version 1.0. U.S. Geological Survey data release. <https://doi.org/10.5066/P9D9S4EY>
- Stein, R., Fahl, K., Gierz, P., Niessen, F., & Lohmann, G. (2017). Arctic Ocean sea ice cover during the penultimate glacial and the last interglacial. *Nature Communications*, *8*(1), 373. <https://doi.org/10.1038/s41467-017-00552-1>
- Stein, R., Fahl, K., Schade, I., Manerung, A., Wassmuth, S., Niessen, F., & Nam, S.-I. (2017). Holocene variability in sea ice cover, primary production, and Pacific-water inflow and climate change in the Chukchi and east Siberian seas (Arctic Ocean). *Journal of Quaternary Science*, *32*(3), 362–379. <https://doi.org/10.1002/jqs.2929>
- Swann, A. L., Fung, I. Y., Levis, S., Bonan, G. B., & Doney, S. C. (2010). Changes in Arctic vegetation amplify high-latitude warming through the greenhouse effect. *PNAS*, *107*(4), 1295–1300. <https://doi.org/10.1073/pnas.0913846107>
- Tarasov, P. E., Andreev, A. A., Anderson, P. M., Lozhkin, A. V., Leipe, C., Haltia, E., et al. (2013). A pollen-based biome reconstruction over the last 3.562 million years in the Far East Russian Arctic—New insights into climate-vegetation relationships at the regional scale. *Climate of the Past*, *9*(6), 2759–2775. <https://doi.org/10.5194/cp-9-2759-2013>
- Thompson, A. J., Skinner, C. B., Poulsen, C. J., & Zhu, J. (2019). Modulation of mid-Holocene African rainfall by dust aerosol direct and indirect effects. *Geophysical Research Letters*, *46*, 3917–3926. <https://doi.org/10.1029/2018GL081225>
- van Kampenhout, L., Lenaerts, J. T. M., Lipscomb, W. H., Lhermitte, S., Nöel, B., Vizcaino, M., et al. (2020). Present-day Greenland ice sheet climate and surface mass balance in CESM2. *Journal of Geophysical Research: Earth Surface*, *125*, e2019JF005318. <https://doi.org/10.1029/2019JF005318>
- Wang, M., Ghan, S., Ovchinnikov, M., Liu, X., Easter, R., Kassianov, E., et al. (2011). Aerosol indirect effects in a multi-scale aerosol-climate model PNNL-MMF. *Atmospheric Chemistry and Physics*, *11*(11), 5431–5455. <https://doi.org/10.5194/acp-11-5431-2011>
- Zender, C. S., Bian, H. S., & Newman, D. (2003). Mineral dust entrainment and deposition (DEAD) model: Description and 1990s dust climatology. *Journal of Geophysical Research*, *108*(D14), 4416. <https://doi.org/10.1029/2002JD002775>
- Zhu, J., Poulsen, C. J., & Otto-Bliesner, B. L. (2020). High climate sensitivity in CMIP6 model not supported by paleoclimate. *Nature Climate Change*, *10*(5), 378–379. <https://doi.org/10.1038/s41558-020-0764-6>

## References From the Supporting Information

- Adler, R., Sapiiano, M. R. P., Huffman, G. J., Wang, J.-J., Gu, G., Bolvin, D., et al. (2018). The global precipitation climatology project (GPCP) monthly analysis (new version 2.3) and a review of 2017 global precipitation. *Atmosphere*, *9*(4), 138. <https://doi.org/10.3390/atmos9040138>